USING ENGINEERING CAMERAS ON MARS ROVERS AND LANDERS TO RETRIEVE ATMOSPHERIC DUST LOADING

A Thesis

by

CHRISTOPHER ALAN WOLFE

Submitted to the Office of Graduate and Professional Studies of
Texas A&M University
in partial fulfillment of the requirements for the degree of

MASTER OF SCIENCE

Chair of Committee,	Mark Lemmon
Committee Members,	Ping Yang
	Ryan Ewing
Head of Department,	Ping Yang

August 2016

Major Subject: Atmospheric Sciences

ABSTRACT

Dust in the Martian atmosphere influences energy deposition, dynamics, and the viability of solar powered exploration vehicles. The *Viking*, *Pathfinder*, *Spirit*, *Opportunity*, *Phoenix*, and *Curiosity* landers and rovers each included the ability to image the Sun with a science camera equipped with a neutral density filter. Direct images of the Sun not only provide the ability to measure extinction by dust and ice in the atmosphere, but also provide a variety of constraints on the Martian dust and water cycles. These observations have been used to characterize dust storms, provide ground truth sites for orbiter-based global measurements of dust loading, and help monitor solar panel performance. In the cost-constrained environment of Mars exploration, future missions may omit such cameras, as the solar-powered *InSight* mission has.

We seek to provide a robust capability of determining atmospheric opacity from sky images taken with cameras that have not been designed for solar imaging, such as the engineering cameras onboard *Opportunity*. Our investigation focuses primarily on the accuracy of a method that determines optical depth values using a scattering model that implements the ratio of sky radiance measurements at different elevation angles, but the same scattering angle. MER engineering cameras are used to obtain non-solar sky images approximately 90° away from a low horizon Sun. A discrete ordinate radiative transfer algorithm and robust atmospheric scattering model are used in conjunction with the downlinked image files to produce both an image and model radiance profile. Optical depth is derived using a least-squares curving fitting routine within the scattering model that iteratively compares the two radiance profiles. Derived optical depth values are then compared against observed Pancam

measurements to assess goodness of fit.

Operational use requires the ability to retrieve optical depth on a timescale useful to mission planning, and with an accuracy and precision sufficient to support both mission planning and validation of orbital measurements. This thesis will present a simulation-based assessment of an imaging strategy and its error budget, as well as a validation based on the comparison of direct extinction measurements from archival Navigation camera (Navcam) data. Results from this observational campaign will follow a preliminary validation that was done using synthetic sky images in order to test the robustness of the scattering model. After the observational results are presented, an in-depth error analysis will provide further detail pertaining to the fidelity of the derived measurements. Finally, this thesis will conclude with a brief discussion regarding the implications of this study and what the future has in store for ground-based optical depth retrieval.

NOMENCLATURE

A	Actinic flux
CAHVOR	Geometric Camera Model
DISORT	Discrete Ordinate Radiative Transfer
DN	Data Number
η	Airmass
EDR	Experiment Data Record
F	Flux
FOV	Field of View
FSW	Flight Software
g	Asymmetry factor
H	Scale height
I	Radiance
I/F	Radiance factor
IDL	Interactive Data Language
JPL	Jet Propulsion Laboratory
L_s	Areocentric longitude
MER	Mars Exploration Rover
Mini-TES	Miniature Thermal Emission Spectrometer
MIPL	Multimission Image Processing Laboratory
MPFIT	Robust non-linear least squares curve fitting program
MY	Mars Year
Navcam	Navigational camera
ω	Single-scattering albedo

Ω	Solid angle
P	Phase function
Pancam	Panoramic Camera, Main Cameras on Mars Exploration Rovers
PDS	Planetary Data System
R	Instrument response
R^*	Measured signal ($^{DN}/_{s}$)
RDR	Reduced Data Record
RMSE	Root Mean Square Error
S	Source function
Sol	A Mars solar day (24 hours 39 minutes 35.244 seconds)
τ	Aerosol optical depth
TES	Thermal Emission Spectrometer
X	Size parameter

TABLE OF CONTENTS

Page

LIST OF FIGURES

FIGURE Page

LIST OF TABLES

TABLE Page

1. INTRODUCTION

1.1 Overview

Robotic spacecraft have been sent to explore and map the surface of Mars since the early 1960's. These missions began as relatively simple science experiments with just a few instruments and gradually evolved into complex machines that would eventually traverse and photograph the surface of the planet. Over the last 50 years, both orbital and ground spacecraft have sent back terabytes of data in the form of sensor measurements and images. As a result, our understanding of both the chemical and physical processes that occur on Mars has dramatically improved.

One particular area of study that has seen significant improvement is the modeling of radiative transfer and energy transport in the Martian atmosphere. With robotic spacecraft constantly making new discoveries and providing a steady stream of data, we now have have a greater understanding of the atmospheric processes that occur on Mars, including those that took place in the past. Particle mean size, imaginary index of refraction, optical depth, and other aerosol properties that are important for atmospheric modeling have been able to be measured to a much higher degree of accuracy with the advent of ground-based spacecraft observations. Subsequently, retrieving these parameters via sky imaging and other indirect means has led to a vast improvement in radiative transfer modeling and our understanding of the role dust plays on Mars.

1.2 The Atmosphere of Mars

Despite having several distinct layers, the Martian atmosphere is quite thin and tenuous with a surface pressure that measures less than 1% of Earth's. The atmosphere is nearly 95% carbon dioxide by weight, with other trace gases such as

nitrogen and argon making up the remaining 5%. Although water is only a minor constituent of the Martian atmosphere, primarily because of low atmospheric and surface temperatures, it plays an important role in atmospheric chemistry and meteorology. Even though the atmosphere measures only 600 Pascals at the surface, it is still thick enough to support a variety of weather phenomenon, including clouds, fog, dust storms, and dust devils, all of which have been observed and studied using both orbital and ground spacecraft. Near the polar ice caps, there is even observational evidence of carbon dioxide snow. This seasonal deposition and release of a large part of the Martian atmosphere at the poles can have a strong influence on global circulation patterns.

1.3 Dust on Mars

In addition to the molecular gasses that make up the atmosphere of Mars, there is also an abundance of dust consisting of small particles of iron oxide and other minerals. The optical properties of Martian dust are dominated by a high content of nanophase or poorly crystalline ferric oxides (Bell et al., 2000; Morris et al., 2006a, 2006b) analogous to terrestrial palagonites (weathering products from mafic volcanic glasses). Data from the MER rovers and previous studies indicate that suspended dust particles within the atmosphere have a radius of roughly $1.5\mu m$ (Pollack et al., 1995; Markiewicz et al., 1999; Tomasko et al., 1999). Their presence is not only responsible for giving Mars its reddish hue, but also significantly affects the thermal structure of the atmosphere due to the dust particles absorbing sunlight, especially at 400 to 600 nm, as well as thermal radiation, especially near $9\mu m$ (Lemmon et al., 2004). Dust particles are also a major driver of atmospheric circulations at all spatial scales. At the microscale level, turbulence plays a large role in the atmospheric dynamics that occur on Mars and is responsible for raising and maintaining the large

quantity of dust found in the Martian atmosphere.

Dust is lifted into the atmosphere by mechanisms such as dust devils (Edgett and Malin, 2001; Greeley et al., 2006, 2010; Moores et al., 2015) or dust storms (Toon et al., 1977; Wolff et al., 1997) and removed again by gravitational settling or turbulent dispersion. Dust storms are common on Mars, especially those that are regional or local in scale, and while they can occur at any time, they are most frequent during spring and summer in the southern hemisphere, when Mars is passing closest to the Sun and surface temperatures are at their highest. This creates favorable conditions for convection to occur, and coupled with Mars' weak gravitational field, allows the dust to remain aloft in the atmosphere. As the dust particles absorb sunlight, they warm the air around them. On a cold planet such as Mars, the air in the immediate vicinity of the dust thus becomes much warmer than the surrounding air. This variation in temperature sets up a strong pressure gradient force that causes the wind to blow faster (Ahrens, 2007). As a result, higher winds pick up more dust, which causes more heating and even stronger winds. Activity is at first local and vigorous, with large amounts of dust thrown high into the atmosphere. In a few days the storm has the potential to obscure the entire surface and reduce visibility to less than 5% of normal. Figure 1.1 shows just how quickly sky opacity may change as a dust storm moves over the *Opportunity* site. The intensification process is short-lived, however, as atmospheric clarity begins to return almost immediately, becoming normal typically in days to weeks (Cantor et al., 2007). Most of the storms are local to regional in extent and last only a few weeks. Storms become planet encircling episodically, averaging once per 3-4 Mars years (Zurek and Martin, 1993).

Dust in the Martian atmosphere not only influences energy deposition and dynamics, but the viability of solar powered exploration vehicles as well. During a relatively clear day, the indirect or scattered component of sunlight remains relat-

Figure 1.1: Time-lapse composite of Martian horizon during Sols 1205 (0.94), 1220 (2.9), 1225 (4.1), 1233 (3.8), 1235 (4.7) shows how much sunlight the July 2007 dust storms blocked; Tau of 4.7 indicates 99% blocked (NASA/JPL-Caltech/Cornell, 2007a).

ively low. When there is lots of dust in the atmosphere, however, the majority of the total sunlight reaching the surface can be indirect. As a result, total irradiance is reduced, thereby weakening solar cell output. Over time, dust settles out of the atmosphere and onto solar panels. This dust blocks and shifts the frequency of the incoming light, further degrading solar cell output. Dust deposition on the solar arrays was measured on the Pathfinder mission to degrade the performance at a rate of 0.28% per sol during the initial 30 sols of the mission (Landis, 2000).

Currently there are five orbiting spacecraft that collect data and continue to

monitor dust aerosols on Mars. A small fleet of landers and rovers including *Viking*, *Pathfinder*, *Spirit*, *Opportunity*, *Phoenix*, and *Curiosity* have also been deployed on Mars to not only explore the surface, but provide ground-based measurements of dust aerosols. Each of the aforementioned landers and rovers included the ability to image the Sun with a science camera that included a neutral density filter. Direct images of the Sun provide the ability to measure extinction by dust and ice in the atmosphere. These observations have been used to characterize dust storms, provide ground truth sites for orbiter-based global measurements of dust loading, and to help monitor solar panel performance (Colburn et al., 1989; Smith and Lemmon, 1999; Lemmon et al., 2004; Lemmon et al., 2015).

1.4 Optical Depth

The radiative impact of the dust on Mars varies with optical depth, a dimensionless parameter that describes the amount of radiation that is scattered and/or absorbed as a beam of incident sunlight travels through a planet's atmosphere. Optical depth can be derived from the Beer-Lambert-Bouguer extinction law, $F = F_0 e^{-\tau\eta}$, where F is outgoing or observed flux near the surface, F_0 is the incident flux at the top of the atmosphere, τ is optical depth, and η is the airmass, which is defined as the optical depth along an arbitrary line of sight relative to that in the zenith direction (commonly approximated as $\sec(\theta)$, where θ is the solar zenith angle). Values of τ less than one indicate an atmosphere where very little sunlight is attenuated, and therefore, most solar radiation is able to reach the planet's surface largely unimpeded. Values of τ greater than one, however, describe an atmosphere where particles absorb and/or scatter most of the incoming solar radiation, leaving very little sunlight that is able to penetrate to the surface.

Generally low and stable opacities signify southern winter (and aphelion), while

high and variable opacities correlate with southern summer (and perihelion) (Lemmon et al., 2015). Atmospheric dustiness may vary considerably through a Martian year, and although there is a general annual trend in dust loading there is also much interannual variability, most significantly in the number and size of dust storms which occur (Newman et al., 2002). While relative variations of optical depth can be readily obtained from remote observations, absolute values are much trickier to obtain because they require accurate knowledge of important properties related to dust, such as the particle size distribution and the optical parameters (Montabone et al., 2015).

Optical depth measuring from landed payloads is a critically important component because of the higher accuracy and precision generally available from such measurements (Lemmon et al., 2015). Unlike Earth, which has a vast network of ground-based monitoring stations, Mars only has two active surface rovers. And while orbital observations allow for a more complete characterization of dust loading over spatial and temporal scales compared to ground based spacecraft, they generally embody more modeling or retrieval assumptions (e.g., Smith, 2004, 2009; Wolff et al., 2009). Despite orbiting spacecraft providing information over large areas of the planet at any given time, they are unable to provide a self-consistent "ground-truth". Obtaining ground-truth measurements are particularly important as they allow for the calibration of remote-sensing data and aid in the interpretation and analysis of what is actually being sensed.

Daily measurements of dust optical depth spanning several Martian years allows for the analysis of interseasonal and interannual variabilities (Montabone et al., 2015). Monitoring optical depth from the surface is particularly useful as it can provide a variety of constraints on the Martian dust and water cycles (Smith, 2003). Retrieving optical depth on a regular basis in this manner can also reveal

patterns which may indicate the presence of water-ice clouds, changes in aerosol concentrations, as well as evidence of dust storm activity (Smith, 2008). In addition, surface-based optical depth retrieval allows ground truthing of orbital measurements, provides a key meteorological variable, provides context for scene imaging, and (for solar-powered missions) allows a valuable engineering assessment of solar panel performance. Generally, landed spacecraft on Mars measure optical depth using direct

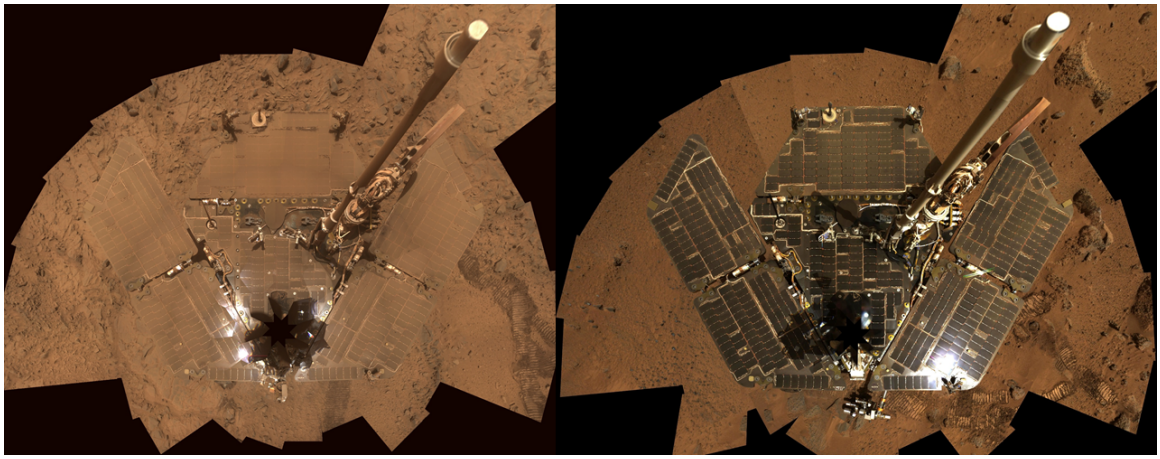

Figure 1.2: Overhead view of MER-A *Spirit's* solar panel deck. The image on the left was taken in October 2007 and shows the solar panels covered in a fine layer of dust, while the image on the right, taken in November 2008, was aquired after a cleaning event (NASA/JPL-Caltech/Cornell, 2006, 2007b).

solar imaging, such as done by Pancam on the MER rovers and Mastcam on MSL. Measuring optical depth in this manner, however, requires dedicated resources. In some cases, these measurements can divert resources away from other priorities. In addition to high resolution science camera(s), rovers and landers typically have low resolution cameras without filter wheels that are part of the engineering package (Maki et al., 2003). Deriving optical depth from non-solar sky images acquired by

engineering cameras, therefore, places fewer requirements on the overall system.

Robotic spacecraft that land on the surface of Mars are subjected to dust and dust deposition. Dust can block and shift the frequency of incoming light, which is problematic for solar powered exploration vehicles as this reduces the output provided by the solar panels. Figure 1.2 is adapted from a NASA/JPL press release and shows *Spirit's* (MER-A) solar panel deck before and after a dust cleaning event. In addition to dust accumulating on the solar panels, it can also collect on the camera optics. This thin layer of dust that forms on the camera window modulates sky brightness and introduces extra extinction and scattering of light into the camera's field of view (FOV), therefore complicating solutions to the radiative transfer equation. In the case of Pancam, one of the cameras on the MER rovers, interpretation of this extinction from the dust on the camera window was operationally significant as the error would interfere with the assessment of the performance of the solar arrays (Lemmon et al., 2015).

The future *InSight* mission, which was originally set to launch in March of 2016, had a MER-like navigational camera at the end of a robotic arm. Its purpose was to capture images of the instruments deployed on the ground and acquire panoramic views of the terrain surrounding the landing site. It also had a FOV identical to the MER Navcam engineering cameras. Unfortunately at the end of 2015, a persistent vacuum failure in the Seismic Experiment for Interior Structure (SEIS) grounded the mission. With a launch now expected in May of 2018, the Instrument Deployment Camera (IDC) located on *InSight's* robotic arm has since received an upgrade, giving it the ability to take color sky images using a RGB microfilter. In addition to making it much easier to see visible differences in sky opacity, color sky images will also provide color ratio, which allows for a better prediction of optical depth.

2. PROCEDURE AND PRELIMINARY VALIDATION

2.1 Radiative Transfer Equation and DISORT

Before optical depth can be derived, sky brightness, as seen from the ground, must be computed first. As a beam of sunlight propagates through a medium, such as the atmosphere of a planet, it is affected by absorption, emission, and scattering processes. The radiative transfer equation describes these interactions mathematically. Below is a compact form of the 1-D diffuse radiative transfer equation applicable to horizontally homogeneous, plane-parallel geometries. On the right hand side is a differential describing the rate at which diffuse radiance (dependent on optical depth, airmass, and azimuthal angle) changes with path optical depth. On the left hand side is the total diffuse radiance minus a source function (also dependent on optical depth, airmass, and azimuthal angle).

$$\eta \frac{dI(\tau, \eta, \phi)}{d\tau} = I(\tau, \eta, \phi) - S(\tau, \eta, \phi) \tag{2.1}$$

The source term on the right of equation 2.1 can be written as follows, where ω is the single-scattering albedo or the ratio of scattering efficiency to total extinction efficiency and P is the phase function, described in more detail on the next page:

$$S(\tau, \eta, \phi) = \frac{\omega(\tau) I_0}{4\pi} P(\tau, \eta, \phi, -\eta_0, \phi_0) e^{-\tau/\eta_0} + \frac{\omega(\tau)}{4\pi} \int_0^{2\pi} \int_{-1}^{1} IP(\tau, \eta', \phi', \eta, \phi) \tag{2.2}$$

The theoretical modeling of light scattering in planetary atmospheres is usually divided into two parts: single scattering by small volume elements in the atmosphere and multiple scattering by the entire atmosphere (Hansen and Travis, 1974). The first term in Equation 2.2 describes single scattering or the diffuse radiation arising

from the scattering of the direct solar beam. The second term accounts for multiple scattering of diffuse radiation. Furthermore, we make a first-order correction for Mars' vertically extended atmosphere ($^{H}/_{R}$, the scale height to radius ratio, is 0.003, causing the plane-parallel assumption to fail near the horizon). Equation 2.1 is evaluated over the line-of-sight for a curved atmosphere, with the direct solar term calculated using spherical geometry. The diffuse radiance term is calculated for a plane parallel atmosphere via a discrete ordinates method (Stamnes et al., 1988). The latter approximation is valid as near-horizon light is only a small part of the actinic flux incident on the dust.

Within the source function is the phase function, a dimensionless quantity that characterizes the scattering process and describes the angular distribution of scattered light. On Mars, the scattering particles are large compared to the wavelength of incident radiation, producing a size parameter (X), or ratio of the particle's radius to wavelength, that lies within the Mie scattering regime. This results in a strongly-forward peaked phase function, which makes it computationally intensive to obtain accurate solutions to the radiative transfer equation. Therefore, the multiple scattering term in the source function is evaluated using a numerical algorithm known as Discrete-Ordinate-Method Radiative Transfer (DISORT). DISORT is a model of the transfer of monochromatic, unpolarized radiation from one location to another by scattering, emission, and absorption in a vertically homogeneous, plane-parallel atmosphere (Shaw et al., 2013). DISORT reduces the radiative transfer equation to a series of independent equations which allows us to solve for the azimuthally resolved intensity field.

DISORT uses the δ-M transformation (Wiscombe, 1977) to achieve optimum computational efficiency and accuracy for strongly forward-peaked phase functions. The essence of the δ-M method is to separate the phase function P into the sum of

a delta-function in the forward direction and a truncated phase function P' which is expanded into a series of Legendre polynomials. As mentioned above, the phase function associated with the scattering of visible and near-infrared radiation by cloud and dust particles on Mars has a pronounced peak in the forward scattering direction primarily due to diffraction. This peak is several orders of magnitude larger than the values of the phase function at side- and back-scattering angles and as a result, requires a large number of expansion terms to accurately reproduce the original phase function. We use 256 expansion terms, or moments, to reconstruct the phase function. This was found to be more than enough to faithfully represent the dust particles. The equation for the truncated phase function is shown below, where M is the total number of Legendre polynomials and g is the asymmetry parameter, specifying the degree of scattering in the forward direction.

$$P(\tau, \cos(\Theta)) = \sum_{l=0}^{2M-1} (2l+1) g_l(\tau) P_l(\cos(\Theta)) \tag{2.3}$$

In DISORT, the scattering phase function depends only on the scattering angle (Θ) between the incident and scattered beams. Therefore, the azimuthal(ϕ)-dependence in Equations 2.1 and 2.2 can be factored out if the phase function is expanded into Legendre polynomials (see Equation 2.3) and the intensity is expanded in a Fourier cosine series (see Equation 2.4). Once the phase function has been expanded using Legendre polynomials, the final step in factoring out the ϕ-dependence, is to expand the intensity in a Fourier cosine series. The azimuthal integration of this series drops all but the $m = 0$ term, therefore producing azimuthally-averaged intensities.

The equation for the expanded intensity is shown below, where once again, M is

the total number of Legendre polynomials used.

$$I(\tau, \eta, \phi) = \sum_{l=0}^{2M-1} I^M(\tau, \eta) \cos(m(\phi_0 - \phi)) \tag{2.4}$$

Substitution of Equations 2.3 and 2.4 into the radiative transfer equation (2.2) causes it to split into $2M$ independent integro-differential equations, one for each azimuthal intensity component so that we now have the following equation:

$$\eta \frac{dI^m(\tau, \eta)}{d\tau} = I^m(\tau, \eta) - S^m(\tau, \eta) \quad (m = 0, 1, ..., 2M - 1) \tag{2.5}$$

A discrete ordinate approximation of the equation above is given by approximating the integral within the source function by a quadrature sum and thus transforms the integro-differential equation into the following system of differential equations where M is the total number of Legendre coefficients used and N is the total number of quadrature angles (streams):

$$\eta_i \frac{dI^m(\tau, \eta_i)}{d\tau} = I^m(\tau, \eta_i) - S^m(\tau, \eta_i) \quad (m = 0, 1, ..., 2M - 1) \quad (i = 1, ..., \pm N) \tag{2.6}$$

For the upward-looking geometry, solutions were calculated using 64 streams, or discrete zenith directions (quadrature angles), and 256 Legendre polynomial moments to represent the angular distributions of atmospheric and surface scattering. The solution of this equation yields the intensity which an observer would detect if an instrument were located in a layer with optical depth τ, and if the instrument were pointed in such a way as to be observing only the radiation propagating along a specific line of sight.

The wavelength dependence of all quantities has been omitted from all the equations in this section as DISORT makes no explicit use of wavelength except in the

calculation of the Planck function, which we chose to ignore. Thus the medium and boundary properties, and the resulting radiant quantities calculated can be regarded as values at a particular wavelength, in this case, the peak spectral responsivity of the Navcam instrument, 650nm (Maki et al., 2003).

We also chose to ignore the effects of Rayleigh scattering as it only slightly modifies the phase function. Opacity from Rayleigh scattering is trivial on Mars for wavelengths near 650nm. Rayleigh scattering by the CO_2 atmosphere accounts for an optical depth that is roughly $(1.2 - 1.6) \times 10^{-3}$ when looking in the red portion of the visible spectrum and, therefore, is negligible when compared to the light scattered by dust particles. It is the resulting Mie scattering from atmospheric dust particles that is primarily responsible for the observed optical depth. Scattering by the fine dust grains suspended in the atmosphere results in an optical depth that can vary dramatically over the course of a Martian year (from 0.37 to 4.6), with a typical, or average, value being approximately 0.78.

For our specific case, we model the atmosphere as one layer with dust acting as the only aerosol and assume no vertical structure. The assumption that this single atmospheric dust layer is uniform is a reasonable approximation in that dust tends to be well mixed through the bottom scale height and moderately well mixed for a few scale heights. Using additional atmospheric dust layers in the modeling process, therefore, will not lead to more accurate results, as the rover on the surface is unable to discern between multiple layers of well mixed dust particles.

A simplified integral form of the radiative transfer equation rewritten in terms of measured signal is shown below:

$$R^* \sim R \left(\frac{\omega \, F \, P \, (\theta)}{4} + \omega \, \langle A \rangle \right) \int_0^{\tau_0} e^{-(\tau_0 - \tau)\eta_0} \, e^{-\tau \eta} \, \eta \, \mathrm{d}\tau \tag{2.7}$$

Where R^* is the signal measured and R is the instrument response (signal/radiance). The first term in the parenthesis represents the single scattering of direct solar radiation and the second term describes the diffuse, or multiple scattering, that takes place in the atmosphere (approximated as proportional to the mean actinic flux). The integral is the path integral over the emission source and describes the amount of extinction. This particular form of the radiative transfer equation is useful to our study because the derived flux of each pixel in the processed images relies on the observed signal (R^*) measured in data numbers per second ($^{DN}/_{s}$).

The raw $^{DN}/_{s}$ values stored in the PDS archived images are directly proportional to the number of photons incident on each CCD pixel during the commanded integration time, modulated by a variety of correctable instrumental effects (Bell et al., 2006). The total $^{DN}/_{s}$ value for an image, therefore, is roughly proportional to intensity. However, for current engineering cameras, the proportionality constant, R, is poorly known and has not received the same subject of rigorous calibration that the science cameras have gotten. This is expected to remain true for future engineering cameras. For example, the *InSight* cameras were integrated onto the spacecraft without such a calibration.

2.2 Methodology

We seek to provide a robust capability of determining atmospheric opacity from sky images taken with cameras that have not been designed for solar imaging, such as lander and rover engineering cameras. Typically optical depth is retrieved through direct solar imaging using a dedicated multispectral science camera with a neutral density filter (i.e. Pancam) and/or through retrievals using infrared spectra taken by the Mini-TES instrument (Smith, 2006). In this study, however, we will investigate the accuracy of a scattering model that derives optical depth using non-solar sky

images acquired by the MER rover's engineering cameras.

Explained in this section is a method for deriving aerosol optical depth without directly imaging the Sun using the ratio of sky radiance measurements at two different elevation angles, but keeping the scattering angle fixed at approximately 90°. This particular approach to retrieving optical depth is useful not only because it has the ability to free up rover system resources, but it avoids reliance on absolute calibration of responsivity, R. Most importantly, however, it is another way to provide a ground truth measurement of optical depth.

We will contrast the intensity derived from sky images at two elevations and the same scattering angle in order to constrain the optical depth. Near the Sun, the phase function strongly varies with the scattering angle and is primarily driven by the particle size distribution, depending little on particle shape. When roughly 90° away from a low Sun, however, the phase function is smooth and the scattering angle is nearly orthogonal to the elevation angle. In this case, the scattering angle controls the phase function and the elevation angle controls the airmass (η). Using this relationship and applying it to sky images that obey the appropriate geometrical criteria, we can derive optical depth using a relatively simple method. For the low optical depth limit, radiance (I) is simply proportional to optical depth (τ) $\times$ airmass (η), but for the high airmass and/or optical depth limit, multiple extinction becomes important. Therefore, in order to reduce errors from absolute calibration in the high airmass and/or optical depth case, we take the ratio of two sky radiance measurements at the same scattering angle, but different elevation angles. Thus, not only is the absolute radiance calibration removed, but the angular variation of the scattering is removed to first order.

The equation below demonstrates the mathematical approach of the ratio method where R^* is the observed signal measured in $^{DN}/_{s}$ and the subscripts a and b represent

two different elevation angles.

$$\frac{R_a^*}{R_b^*} \approx \frac{\int_0^{\tau_0} e^{-(\tau_0-\tau)\eta_0}\, e^{-\tau\eta_a}\, \eta_a \, \mathrm{d}\tau}{\int_0^{\tau_0} e^{-(\tau_0-\tau)\eta_0}\, e^{-\tau\eta_b}\, \eta_b \, \mathrm{d}\tau} \tag{2.8}$$

Since R^* is proportional to radiance (I), the left-hand side of Equation 2.8 may be rewritten such that the ratio of light intensity at two different elevation angles corresponds to a specific optical depth value. We assume that optical depth remains the same regardless of elevation angle and that it is the airmass, η, that varies with the viewing angle. Variations within the line of site tend to be $< 5\%$ (Lemmon et al., 2015) This information may then be used to produce a brightness profile like the one seen in Figure 2.2. Constructing a brightness profile allows for the prediction of optical depth if intensity ratio is known, or vice versa. More importantly, however, it informs us of the correlation strength between the two parameters.

2.3 Model Description

In addition to the ratio method described in the previous section and the radiative transfer algorithm DISORT, a parameterized dust light-scattering model from (Tomasko et al., 1999) is used and supplemented by parameters from (Johnson et al., 2003) to describe the optical properties of the dust particles in the Martian atmosphere. This treatment of light scattering by randomly oriented, irregularly shaped particles uses a combination of Mie theory, physical optics, geometrical optics, and parameterization (Pollack and Cuzzi, 1980). For the particular geometrical setup outlined in this thesis, the observed sky brightness originates from sunlight scattered by dust particles into the line-of-sight of each pixel, and thus depends primarily on a variety of scattering parameters which are summarized in Table 2.1. While the modeled single-scattering properties of a distribution of particles has been shown to

Table 2.1: Parameters used by the scattering model to derive bulk optical properties of the dust aerosols present in the Martian atmosphere. Included within the table are the range of values the parameters were varied over as well as truth values acquired from previous literature.

Scattering Parameter	Range Varied Over	Truth Value*
Mean Radius (μm)	0.50-2.94	1.6
Variance of Radius	0.200-0.899	0.2-0.5
Imaginary Index of Refraction	0.5013-1.999$\times 10^{-3}$	0.00211
Tomasko 'G' Parameter	50.03-199.99	70
Tomasko 'θ_{min}' Parameter	120.08-209.97	145
Optical Depth	0.200-2.998	0.528
Ground Reflectivity	0.20008-0.34999	0.25
Scale Height (km)	8.501-12.497	10.5

*From Tomasko et al. (1999) and Johnson et al. (2003)

be insensitive to the specific function used to describe the size distribution of the particles, a modified-gamma distribution function described by Hansen and Travis (1974) is used in this thesis. We begin with a size distribution of spheres with radii that have been chosen to have volumes equal to that of the irregular particles for two regimes (small particles and large particles). We also adopt a convention similar to the one used by Pollack and Cuzzi (1980), in which a size parameter less than some upper bound results in Mie theory being used to calculate both the scattering cross section and phase function. For larger particles ($X > 5$), appropriately scaled Mie theory results are used to define the scattering cross section and the phase function is constructed from the sum of 3 components: diffraction, external reflection, and internal transmission (Pollack and Cuzzi, 1980).

For the particles within the large size regime, the diffraction component is assumed to be that of an opaque circular disk having an area equal to the irregular particle's projected area (Pollack and Cuzzi, 1980). The external reflection component for large particles results from a randomly oriented ensemble of convex, irregularly

shaped particles reflecting light incident on their surfaces in precisely the same manner as an ensemble of equal area spheres with the same index of refraction (van de Hulst, 1957; Hansen and Travis, 1974; Hodkinson, 1963). The internal transmission component is primarily responsible for the deviation in the scattering behavior of irregular particles from that of their spherical counterparts (Pollack and Cuzzi, 1980). These three components for large particles, along with the results from Mie theory for smaller particles, are use to obtain a composite phase function.

The shape of the phase function at small scattering angles is determined primarily by diffraction and external reflection and is therefore not significantly affected by particle irregularity. The main deviation in the scattering behavior of large, irregular particles from spheres arises in that component which is internally transmitted and refracted (Pollack and Cuzzi, 1980).

The single scattering parameters shown in Table 2.1 and used in the scattering model are derived, in part, from their size distribution. These parameters include the mean radius (effective particle size) and variance of radius, imaginary index of refraction (measure of how much light a particle absorbs/attenuates), Tomasko 'G' and 'θ_{min}' (2 parameters describing the shape of the phase function), optical depth, ground reflectivity (fraction of incident radiation reflected by the ground), and scale height, which represents the vertical distance above the surface at which the density or pressure of the atmosphere decreases by exactly $1/e$. For larger particles, the Tomasko 'G' parameter, which is related to the slope of the natural log of the phase function for internally transmitted light, and the Tomasko 'θ_{min}' parameter, or the scattering angle at which the log of the phase function reaches a minimum value, are used to collectively describe the shape of the phase function.

The values derived for effective particle size in the literature range from 0.2μm from ultraviolet observations (Chylek and Grams, 1978) to 2.75μm (Toon et al., 1977)

from observations at thermal wavelengths. At wavelengths in the visible and near IR the variance of the size distribution determined by various authors also varies considerably, from 0.2 from Phobos observations (Korablev et al., 1993) to 0.5 or larger (Pollack et al., 1995).

Within the scattering model is a section that truncates out information stored in elevation angles less than 15°. This reduces the chance of the Martian terrain obscuring sky images and the importance of the vertical distribution of dust. This also allows us to ignore the effects of spherical geometry, which can be quite complex to model. The atmospheric scattering model is relatively insensitive to the specific form or details of the surface scattering function. Therefore, below this elevation angle we assume the ground essentially acts as a Lambertian surface.

Once the user provides input values for the single scattering parameters described above, the scattering model then calculates the volumetric or bulk optical properties of the particle size distribution, including the scattering coefficient and average phase function. These outputs provided by the scattering model, along with several additional input parameters, will then be used by the DISORT radiative transfer program to calculate diffuse sky radiance.

2.4 Preliminary Validation and Results

A preliminary validation was done to test the robustness of the ratio method given uncertainty in scattering parameters. In order to recreate the Martian sky and simulate the rover imaging the sky, a database of synthetic sky images or set of truth models with randomly-varied scattering parameters (see Table 2.1) was generated. These images would make up the 'actual' sky conditions on Mars and have units of I/F. A database with a new set of randomly-varied parameters, or assumed conditions, was also generated in order to simulate the rover acquiring

images of the observed sky.

Once the above steps were completed, sky radiance values obtained from DISORT were used to simulate looking at the near horizon sky 90° away from the Sun. The scattering model lets the user tune various geometrical properties, thereby allowing one to view and select sky radiance values from two different elevation angles, while still keeping the scattering angle fixed. This essentially allowed us to control the 'rover's camera' and point it in any direction in the computer generated sky images.

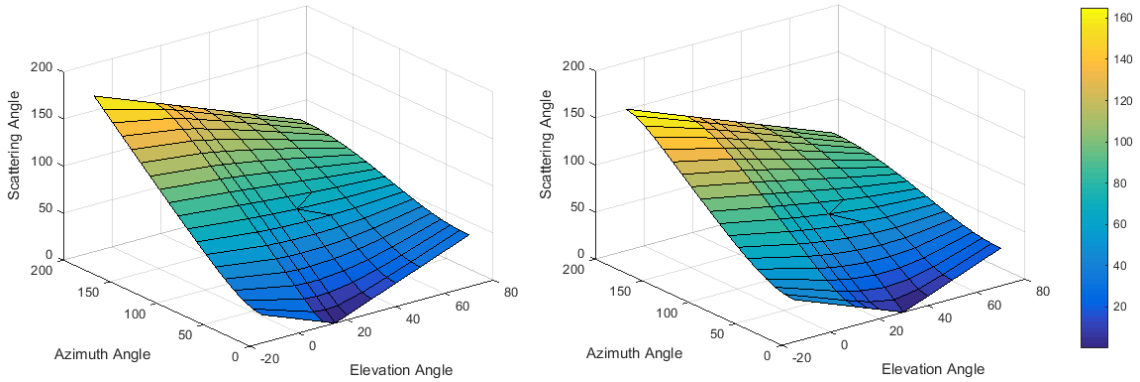

Figure 2.1: Gridded model sky showing the range of scattering angles for elevation angles of 15° (left) and 30° (right). Sky was divided into cells that measured 10° in both azimuth and elevation. Each cell then had the scattering angle computed for the given azimuth and elevation angle of the model sky. Scattering angles near 90° are represented by shades of green.

Using information contained within the database of synthetic sky images, two arrays (a Sun and sky unit vector) were created in which the model sky was divided into "cells" that were 10° in azimuth and elevation. In order to find the scattering angles within the model sky, the dot product between the Sun array and the sky array was computed. With the Sun centered at 0° azimuth and near the horizon with a solar

elevation angle of 20°, scattering angles for the model sky were computed for elevation angles of 15° and 30°. This allowed for the plotting of the preliminary results obtained from the synthetic sky images against a constant scattering angle of 90°. Figure 2.1 shows the gridded model sky with the range of possible scattering angles for the two different elevation angles. After the synthetic sky images were prepared and had the

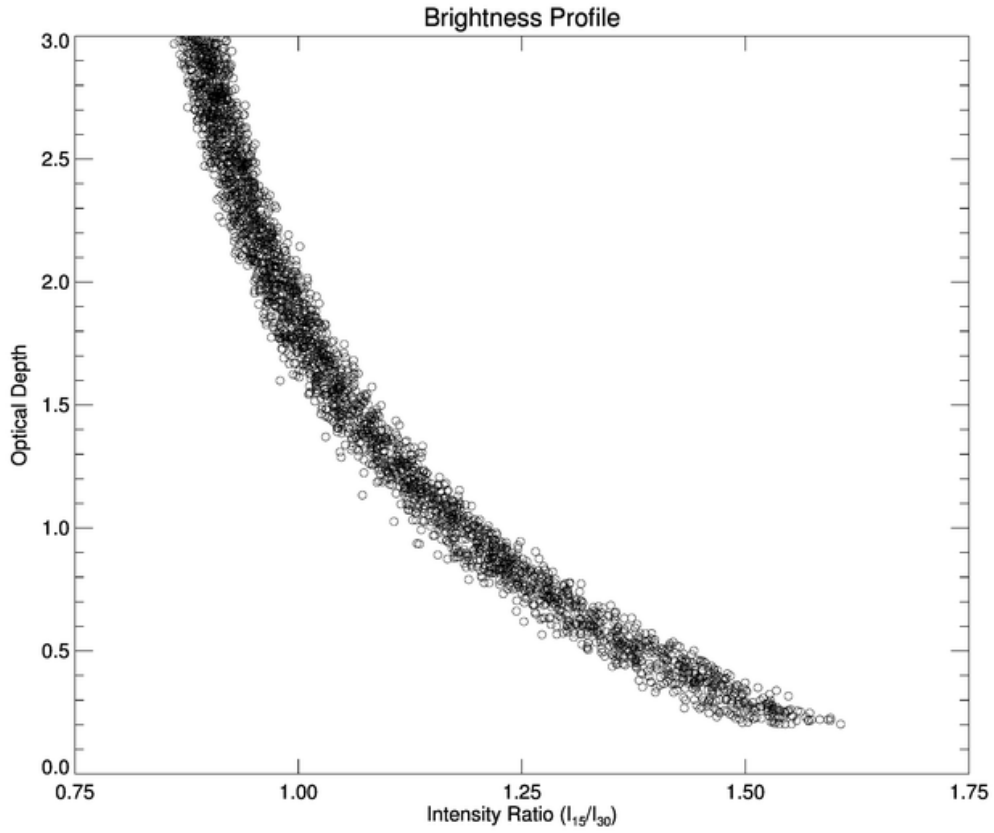

Figure 2.2: Brightness profile resulting from the preliminary validation. It shows the model radiance ratio vs. the optical depth that got that ratio. Each individual data point corresponds to a single synthetic sky image that was constructed from user defined, randomly varied scattering parameters.

correct viewing geometry applied, the scattering model evaluated the images via the ratio method. In this model vs. model analysis, the "assumed" conditions represent the model output from which optical depth was derived from. The ratio method used herein is a simplification: one can gain accuracy using an elevation (ϵ) profile of $d\ln(I)/d\epsilon$ from a sky image, taken at constant scattering angle. This method is analogous to acquiring multiple Sun images at different elevation angles in order to calibrate solar optical depth.

The preliminary results generated using the ratio method and database of synthetic sky images are shown in Figure 2.2. For each of the 3,000 computer generated images, a ratio of sky radiance was calculated and compared with the corresponding opacity that got that ratio in order to construct a brightness profile. Even with random errors in single scattering that are large compared to uncertainties, the model still results in a strong correlation of radiance ratio with optical depth across the range of parameters. It is important to note that 95% of all visible optical depths on Mars are < 1.5 and that using a $d\ln(I)$ profile increases sensitivity.

The spread in the data indicates the effect of varied parameters with the general trend indicating the predictability of optical depth. Low sky opacities are relatively well constrained while higher opacities are less well constrained when using the specific elevation angles of 15° and 30°. Higher opacities become better constrained when using other angles (eg. 25° vs. 40°), hence the process of fitting all angles, not just using a ratio when we look at observational data.

3. OBSERVATIONAL VALIDATION PLAN

3.1 MER Rover and Navigational Camera (Navcam)

The Mars Exploration Rovers *Spirit* (MER-A) and *Opportunity* (MER-B) arrived on the surface of Mars January 4 and 25 of 2004 respectively. *Spirit* landed in a region of Mars known as Gusev Crater and *Opportunity* at a site designated Meridiani Planum. Both sites are located close to the equator of Mars, where temperature and temperature variations are less extreme. Each rover is powered by a triplejunction solar array and equipped with a science payload that includes a variety of instruments including sensors, detectors, spectrometers, and cameras. The main scientific objective of the rovers was to explore their respective landing sites for evidence of past surface water and to assess past environmental conditions at those sites and their suitability for life (Squyres et al., 2003). While *Spirit* is no longer operational, *Opportunity* continues to traverse the surface of Mars, providing new images and data on a regular basis.

Operating a surface rover is an image intensive process. Due to time delays between Earth and Mars, it is impossible to communicate with and control the rovers in real time. The free-roaming nature of the rovers, therefore, requires the daily acquisition and downlink of stereo image data in order to operate and safely drive the vehicle (Maki et al., 2003). Image data from the onboard cameras is quickly analyzed in order to select new targets based on scientific merit, assess the possible traverse options, and command the rover to drive to the designated target. After the rover has completed the traverse, additional image data is used to verify the post-traverse location of the vehicle relative to the commanded location (Maki et al., 2003). Each MER rover has a total of 10 cameras, 6 of which are designated

as engineering cameras and support the operation of the vehicles on the Martian surface.

The Navigation cameras (Navcams, two per rover) are a mast-mounted stereo pair each with a 45° square field of view (FOV) and an angular resolution of 0.82 milliradians per pixel (mrad/pixel) (Maki et al., 2003). The cameras have a small aperture opening ($f/12$) with a focal length of 14.67 mm. The depth of field of the Navcam camera ranges from 0.5 m to infinity, with best focus occurring at 1.0 m. The Navcams use a combination of filters (Schott OG590, KG5, and an ND1.3) to create a red band-pass filter centered at 650nm (Maki et al., 2003). They are primarily used to acquire images of the local terrain and Martian landscape, which are then evaluated upon downlink to help in the navigation of the rover. In addition to providing terrain context for traverse planning, images from Navcam are also used to aid in Pancam and Mini-TES pointing.

While the FOV of the Navcams allows the instrument to observe a larger portion of the sky at once compared to Pancam, it also means that Navcam pointing is more restricted so as to minimize high levels of stray light entering the optics (Moores et al., 2015). Thus, for good results, more angular clearance needs to be kept between the selected sky location and bright targets, such as the sun. In order to help reduce internally relected or scattered stray light from entering the optics, the MER rovers are equipped with a sunshade baffle that surrounds the Navcam intstrument. Over time, ground based spacecraft on Mars get dusty. While wind can occasionally provide a cleaning event, any system needs to be robust against dust contamination of the optics. Dust that settles on the optics may result in camera artifacts, which can be made worse by instrumentally reflected light or shadows cast by the window baffle. To reduce the chances of camera artifacts appearing, Navcam is only aimed $> 60°$ away from the Sun in order to keep direct sunlight off the optics.

3.2 Data Acquisition

All images used in this thesis are from the Planetary Data System (PDS), which archives and distributes scientific data from NASA planetary missions, astronomical observations, and laboratory measurements. PDS archives raw images, or images that have undergone no camera model linearization or radiometric correction, in a standard format called the Experiment Data Record (EDR) (Eliason et al., 2009). The files contained in the EDR archive volume have attached PDS labels identifying and describing the objects within the file. The labels also contain descriptive information needed to interpret or process the data objects in the file.

In addition to a PDS label, Navcam images have a descriptive product identifier (PRODUCT_ID) that includes a sequence identifier, a spacecraft clock time at the time of image acquisition, as well as site and location identifiers. An example of a PRODUCT_ID is 1N451342530EDNCCQOP1567L0M1, where '1N' indicates *Opportunity's* Navcam instrument, '451342530' is a 9-digit time stamp, 'EDN' indicates a downsampled EDR, 'CCQO' is a location identifier, 'P1567' represents a sequence identifier, 'L0' indicates left camera with 0 specifying no filter was used, 'M' is the producer code, and '1' indicates the version number.

Non-solar Navcam sky images were captured with the appropriate geometry (i.e. 20° solar elevation angle and 90° scattering angle) beginning February 17, 2014 as part of a dedicated campaign to create a detailed optical depth validation record that could be used to aid the future *InSight* mission. Included in this campaign are a set of observations which were given the name 'navcam_insight_tau_pm'. This particular observational sequence, illustrated by Figure 3.1, commands the Navcam engineering camera to take a series of 5 sky images. Starting at an azimuthal angle of 0°, an image with the Sun centered in the frame is acquired. The rover then rotates its

mast assembly, acquiring a 2×2 mosaic, with one pair west of north and the other east of north. Each pair of images was separated from north by approximately 20°. Note that the Sun image contains saturation artifacts as well as sky and instrumental scattered light. The purpose for having multiple images was to make sure the right

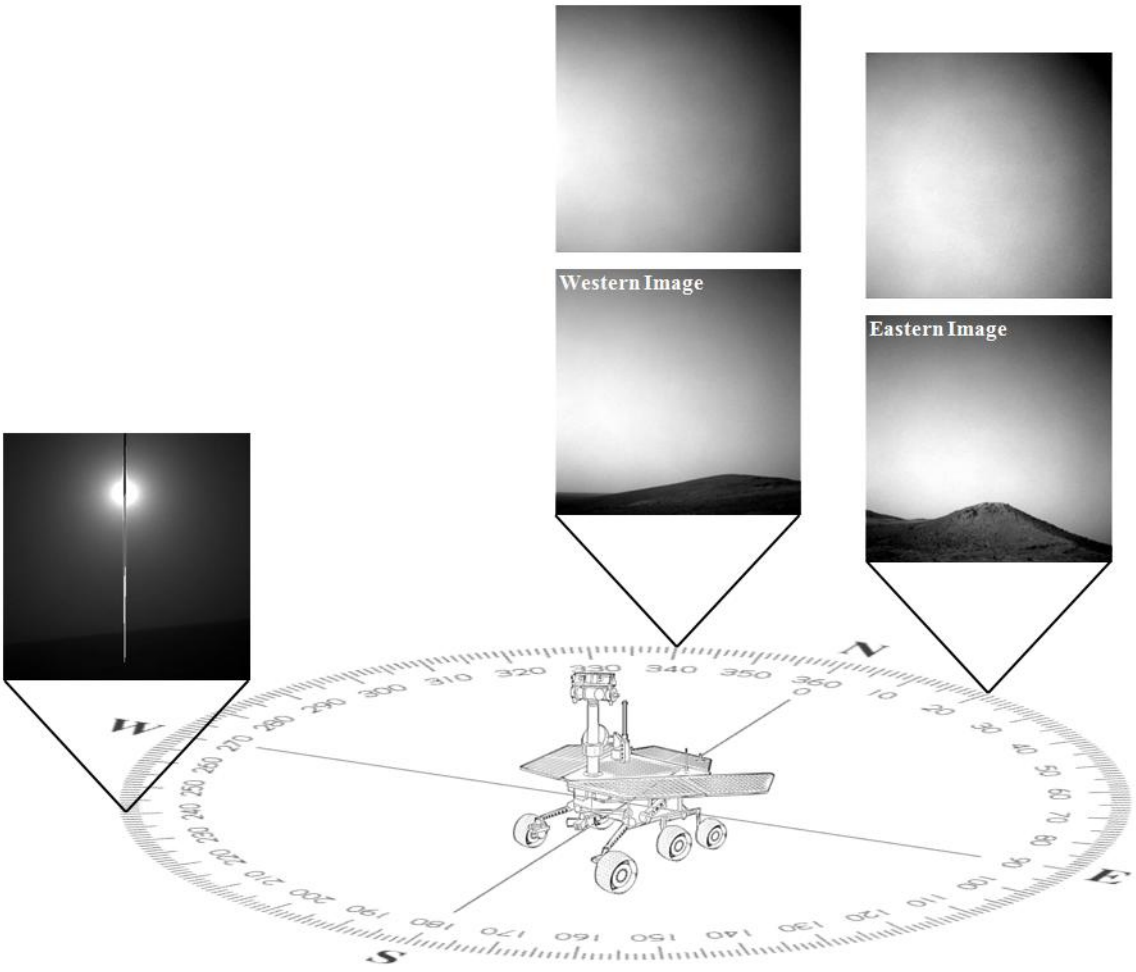

Figure 3.1: Visual representation of the Navcam *InSight* tau sequence executed by *Opportunity* showing the directionality of both western and eastern images. The sky images were captured with the camera facing approximately 90° away from north, acquiring one pair west of north and the other east of north. Images shown in figure were taken on sol 4034.

data could be acquired even if changes to the procedure were made. Only one of the five images, however, is used in the derivation of an optical depth value. The 'extra' images that are not used by the scattering model are an artifact of designing the sequence so that it was robust against seasonal changes given operational constraints. Figure 3.2 provides several examples of the type of images that were used in this

(a) (b) (c)

Figure 3.2: Examples of *Opportunity* Navcam non-solar sky images acquired on sol (a) 3848, L_S=237.5°, (b) 3640, 119.5° and (c) 3733, 167.4°.

study. All images shown were acquired by *Opportunity's* Navcam instrument: (a) is a typical or 'normal' Navcam sky image, (b) is partially contaminated by patchy clouds, and (c) is contaminated by the way the sunlight hits the Navcam optics. The majority of images acquired by the rover resemble (a). A few images downlinked contained cloud formations like those observed in (b), which are likely the reason for the small spikes observed in the Navcam optical depth record seen in Figure 4.5 on page 41. The scattering model assumes a uniform sky of equal brightness, and therefore, has difficulties interpreting discrete cloud formations. Several images were also contaminated by the window baffle that shadows the optics and look similar to

(c). In this case the Sun casts a shadow onto the window, which becomes visible due to the dustiness. Since light scatters off the dust on the window regardless of the viewing angle, we are interested to see if this substantially affects the ratio if the Sun is not shining directly on the optics.

3.3 Radiometric Calibration

Each MER rover payload instrument acquires unique data that is saved onboard as separate products. Upon transmission to Earth, the products are split into parts and packaged inside telemetry packets. Each packet is identified according to the type of data it carried, plus additional ancillary information required for data product reconstruction on the ground (Alexander et al., 2006). The Multimission Image Processing Laboratory (MIPL) analyzes the telemetry data product to create a first order, or 'raw', EDR image. Each MER EDR contains the instrument data reformatted into a usable product, plus a complete label that is fully compliant with PDS rules and guidelines, making the EDR archive-ready (Alexander et al., 2006).

A full-frame, uncompressed raw image file from a MER camera is $1024 \times 1024 \times 12$ bits, or 1.5 megabytes in size. Because the onboard flash memory available for data storage is only 256 megabytes, of which 200 megabytes is available for instrument data storage, the maximum number of full-frame, uncompressed images that can be stored in memory is approximately 130 (Soderblom, 2007). This is roughly equivalent to 2 weeks of downlinked image data at the nominal downlink rates of 100 Mbits/day (Maki et al., 2003). To work within these constraints, the MER imaging system provides the capability to produce additional, less volume-intensive image data products.

The Flight Software (FSW) has the ability to perform certain image processing tasks onboard the rovers in order to both maximize storage efficiency and maintain a

level of image integreity. We use data that has been reduced from 1024×1024 to 512× 512 by pixel averaging, had 12-bit raw data scaled to 8-bit data for communication relay via a look-up table (square-root compression), and compressed images with a moderate quality setting. On the ground, images were radiometrically corrected by removing the effects of exposure time and temperature, and applying a flat-field correction to remove known camera artifacts.

3.4 Geometric Reduction

Before the observed intensities of the Martian sky can be compared with model calculations, the viewing and illuminations geometries of the observation, or where the rover's camera was pointed relative to the Sun, must be known. The incidence (i), emission (e), and scattering (θ) angles must first be derived for each pixel in the Navcam images. Derivation of these observing geometries is a relatively simple process in which knowledge of the rover's orientation, the solar incidence vector centered on the rover (known as the SITE_FRAME) in a Martian surface reference frame, and the pointing information of the camera in the reference frame of the rover (known as the ROVER_FRAME) are extracted from the image's PDS label.

The MER Navcam geometric camera model described by Maki et al. (2003) employ the CAHVOR (Center, Axis, Horizontal, Vertical, Optical, and Radial) projection model developed by Yakimovsky and Cunningham (1978) and Gennery (2001). This model uses five three-dimensional vectors that describe the camera geometry and a set of 3 numbers that describe radial distortion in order to calculate the pointing vector of each pixel in an image. Using the CAHVOR camera model allows a point in XYZ space to be traced into the image plane. The model also includes corrections for geometric distortions in the camera optics, including any radial distortions (Maki et al., 2003).

Once an image is acquired in-flight, MIPL is used to evaluate the downlinked telemetry data packets belonging to that image and compute the CAHVOR model components in what is known as the ROVER_FRAME. These components are stored in the MODEL_COMPONENT entries of the GEOMETRIC_CAMERA_MODEL section of each standardized PDS label (Soderblom, 2007). To transform the pointing vector of each pixel in the image from ROVER_FRAME to SITE_FRAME (i.e., azimuth and elevation relative to the surface of Mars) the rover's absolute position in SITE_FRAME is used (Soderblom, 2007). This information is recorded as an array of four values that specify the rotation of the coordinate system in the ORIGIN_ROTATION_QUATERNION header entry in the ROVER_COORDINATE_SYSTEM section of the PDS label. By using an image's CAHVOR model and the rover's absolute position at the time the image was acquired, azimuth and elevation angle can be calculated for each pixel in the image.

4. MODEL APPLICATION AND RESULTS

4.1 Model Application

Once the radiometrically calibrated images have been geometrically reduced, the sky radiance can be computed for a particular direction for each individual pixel in the image according to the observed viewing geometry. This geometric information is then also relayed to the radiative transfer model so that model sky images can be reconstructed using the appropriate geometry. In the case of this study, we are interested in modeling sky brightness from non-solar Navcam sky images that exhibit elevation angles greater than 15° and scattering angles roughly 90°. Discussed below is the application of the scattering model and minimization algorithm employed to obtain sky brightness.

In addition to the geometric parameters derived from the CAHVOR camera model components, sol, solar elevation angle, solar azimuthal angle, and radiance are extracted from the calibrated images and image headers. The geometric information, along with a variety of setup parameters discussed in Section 2.3, are then used as input to an atmospheric scattering model. The scattering model simulates a random size distribution of irregularly shaped dust particles to produce a bulk (average) phase function. This phase function is then imported into a radiative transfer program to model sky brightness in the form of radiance factor (I/F) according to the image geometry. Following the steps above, the output from the radiative transfer model is then compared to the radiance (I) data from the image file. The comparison is done iteratively, changing optical depth using MPFIT, an optimizer designed for non-linear least-squares curve fitting using the Levenberg-Marquardt technique (Markwardt, 2009). By changing optical depth and leaving the remaining

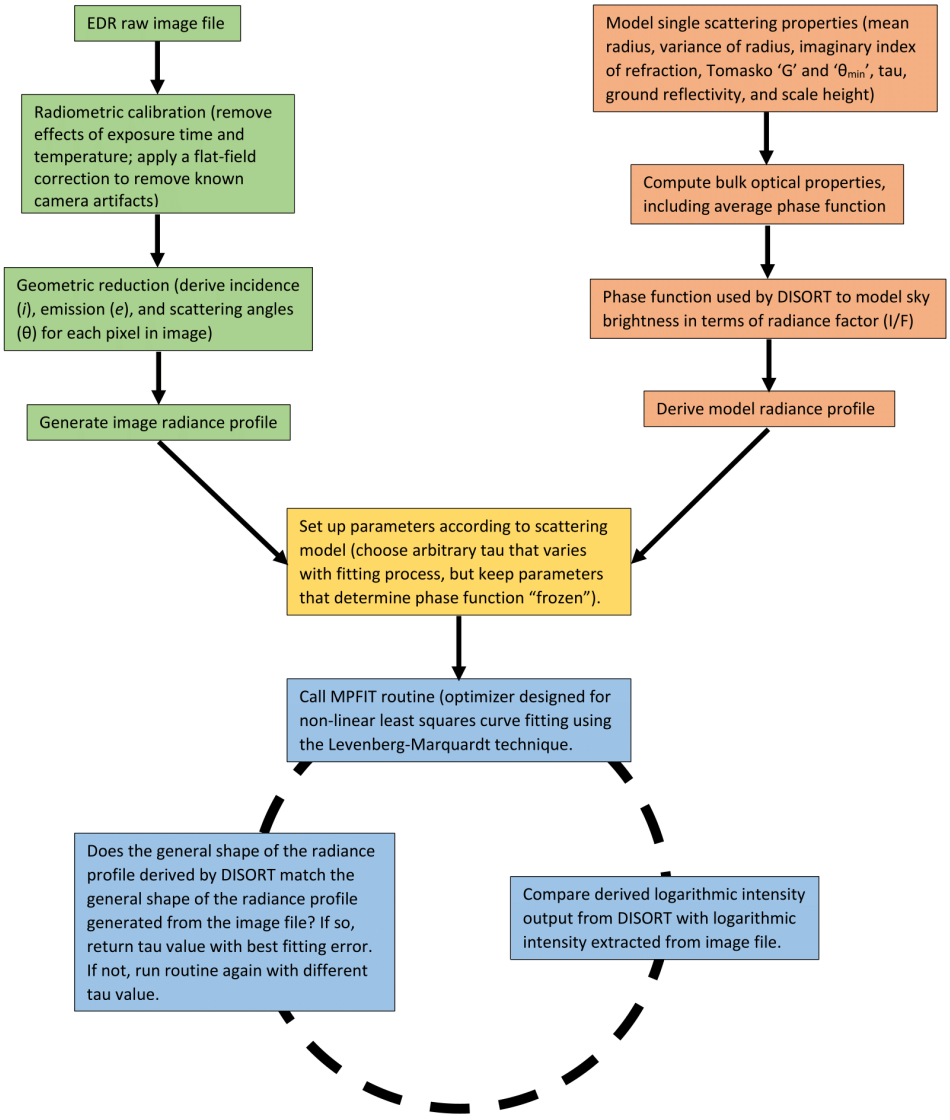

Figure 4.1: Block diagram illustrating the steps taken to arrive at a derived optical depth value from a raw image file. The different colors group together various processes that make up the overall procedure: green corresponds to steps relating to the image file, orange blocks go with the scattering model, the yellow block represents important setup parameters, and the blue blocks represent the iterative process conducted by the MPFIT routine within the scattering model.

single scattering parameters fixed, one alters the resulting radiance profile generated by the radiative transfer program. The idea behind this process is to find the optical

depth that results in a radiance profile that matches, or comes close to matching, the radiance profile from the image file. The modeling process and the steps taken to get from a raw image file to a derived optical depth is summarized in Figure 4.1.

The MPFIT code is based upon the well-known and tested MINPACK-1 FORTRAN minimization library (Moré et al., 1984). The features of MPFIT include the ability to bound parameter values, to control step sizes, and to calculate either one-sided or two-sided numerical derivatives for the Jacobian. The figure of merit for convergence is the traditional χ^2 statistic weighted by the observational errors. The retrieved parameter uncertainties are calculated directly from the diagonal of the covariance matrix (Moré et al., 1984).

The inputs for MPFIT include the function to be minimized, shown by Equation 4.1, and an array of starting values for each of the parameters of the model. In this case, 'model' is the radiance profile generated from DISORT and 'data' is the radiance profile extracted from the image file. Also included within Equation 4.1 are the variables N, or total number of observations, h, a scaling factor chosen to minimize χ^2 for each model parameter, which thus aids in fitting the modeled data to the shape of the curve, and w, a weighting factor related to observational errors. The input parameter tau (optical depth) is allowed to vary throughout the curve-fitting process, while the remaining parameters that determine the phase function are kept "frozen".

$$\chi^2 = \frac{1}{N} \frac{\sum_{j=1}^{N} h \left[model(I/F)_j - data(I)_j \right]^2 w_j}{\sum_{j=1}^{N} w_j} \tag{4.1}$$

MPFIT is used to fit the modeled data from DISORT to the observed radiances from the image file by adjusting optical depth. By looking at the average intensities of both outputs starting at the zeroth moment, MPFIT evaluates the error at each

quadrature angle, minimizing slope errors by varying opacity, until it reaches a global minimum. If a best fit is not found, the routine starts over choosing new starting parameters and repeats the curve-fitting process again. Once a best fit is found, the error is returned along with a corresponding optical depth value for the sky radiance profile. Figure 4.2 illustrates the comparison of model data with the observed data

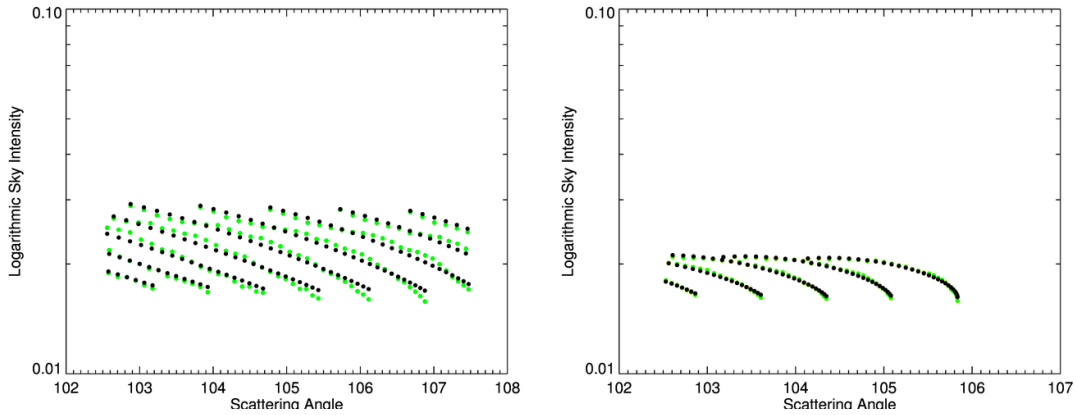

(a) Model vs. image radiance profile for sol 3640.

(b) Model vs. image radiance profile for sol 4012.

Figure 4.2: Output from scattering model showing a 1° azimuth and elevation grid sampled from the image file and calculated within the model. Image sky is show in black with the model sky in green for both cloudy conditions (a) and clear skies (b).

using the MPFIT routine. The apparent pattern is a 1° azimuth and elevation grid, sampled from the image and calculated in the model. The logarithmic sky intensity for each grid point in the image file (black) is compared against the logarithmic sky intensity computed using the model data (green) for the same set of grid points. The image on the left demonstrates the effect clouds have on the model derived sky brightness, whereas the image on the right is a 'typical' or clear sky frame. In both cases, the model still manages to produce a radiance profile that is in close agreement

with that observed from the image file.

4.2 Results

The low-sky images taken by Navcam span an elevation range of roughly 30-45° with azimuthal angles that are nearly perpendicular to the Sun's location in the sky. This was done in order to reduce instrumentally reflected sunlight and replicate the geometry outlined in the model description. Optical depth was modeled from the images using the resulting brightness profile at constant scattering angle. The derived optical depth values were then compared to daily, solar-imaging optical depth measurements from Pancam (Lemmon et al., 2015) to evaluate goodness of fit. Using the same sol range as the Navcam observations, the average uncertainty of the Pancam opacity data set was found to be 0.058. While this is considered fairly typical for error during this particular sol range, it is high for the data taken as companion to the Navcam *InSight* tau sequence. For example, the optical depth acquired by Pancam on sol 4034 is 0.853 ± 0.062 near noon, but 0.827 ± 0.028 70 seconds after the Navcam *InSight* tau is acquired. This is normal, however, and to be expected, as the uncertainty is controlled by airmass.

The scattering model performed an iterative comparison of 37 Navcam images spanning approximately one Martian year. In order to guarantee a near-90° scattering angle without adding to the operational complexity of the rover, a mosaic acquired 2 images for each desired image, where one, depending on the season, was either too far west or too far east (i.e. western images had the correct angle in the northern hemisphere spring/summer, the eastern images did so in the northern hemisphere fall/winter). The 37 additional images also had sky brightness modeled and were analyzed for completeness. Using I/F values from DISORT and the MPFIT routine embedded within the scattering model, optical depth was derived for

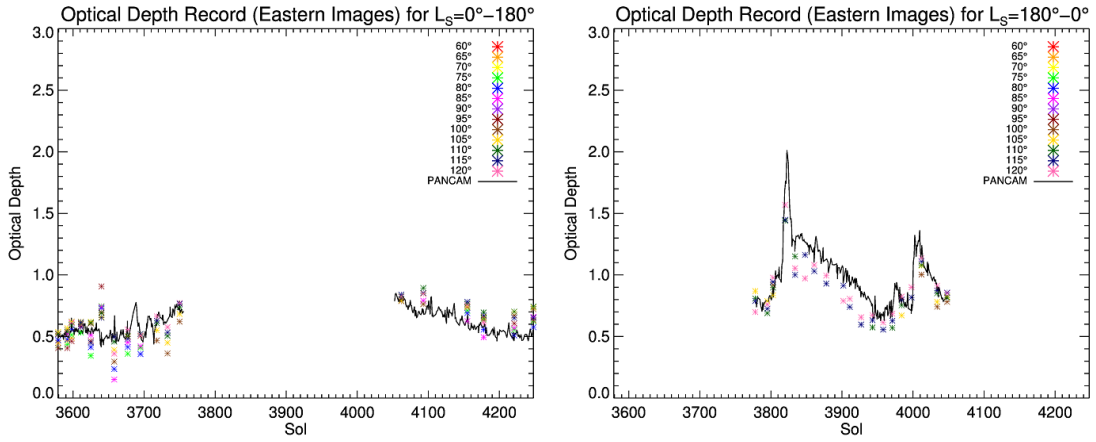

(a) Derived optical depth values from eastern Navcam images for both northern hemisphere spring/summer (left) and fall/winter (right).

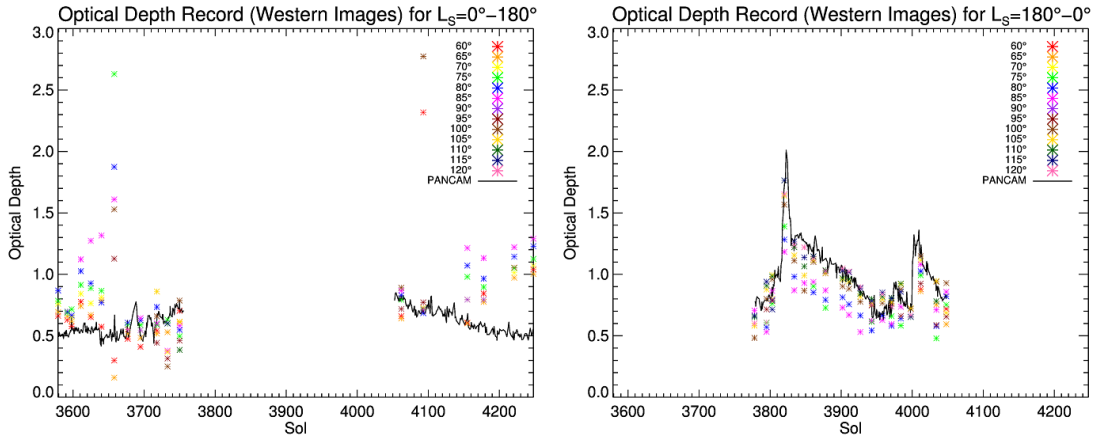

(b) Derived optical depth values from western Navcam images for both northern hemisphere spring/summer (left) and fall/winter (right).

Figure 4.3: Derived optical depth values obtained from scattering model for sols 3579-4248. Sky opacity was derived for a range of scattering angles ($60-120°$) and compared against observed Pancam values (black line) for both dusty ($L_S = 180-0°$) and dust-free ($L_S = 0-180°$) seasons. The top left and bottom right plots are used in the construction of a complete optical depth record.

scattering angles ranging from $60-120°$. This information is presented in Figure 4.3 and shows the importance of maintaining an appropriate angular separation between the Sun and camera line of sight. To determine which scattering angle produced the

best results, an in-depth statistical analysis was applied to the data set. For each scattering angle variance, standard deviation, RMS error, and a reduced χ^2 value were computed. From these statistical tests, it was found that a scattering angle of 105° resulted in a derived optical depth with the best fit when compared to the Pancam data set that was taken in conjunction with the Navcam data on the same sol. RMS error as a function of scattering angle, with Pancam providing the observed

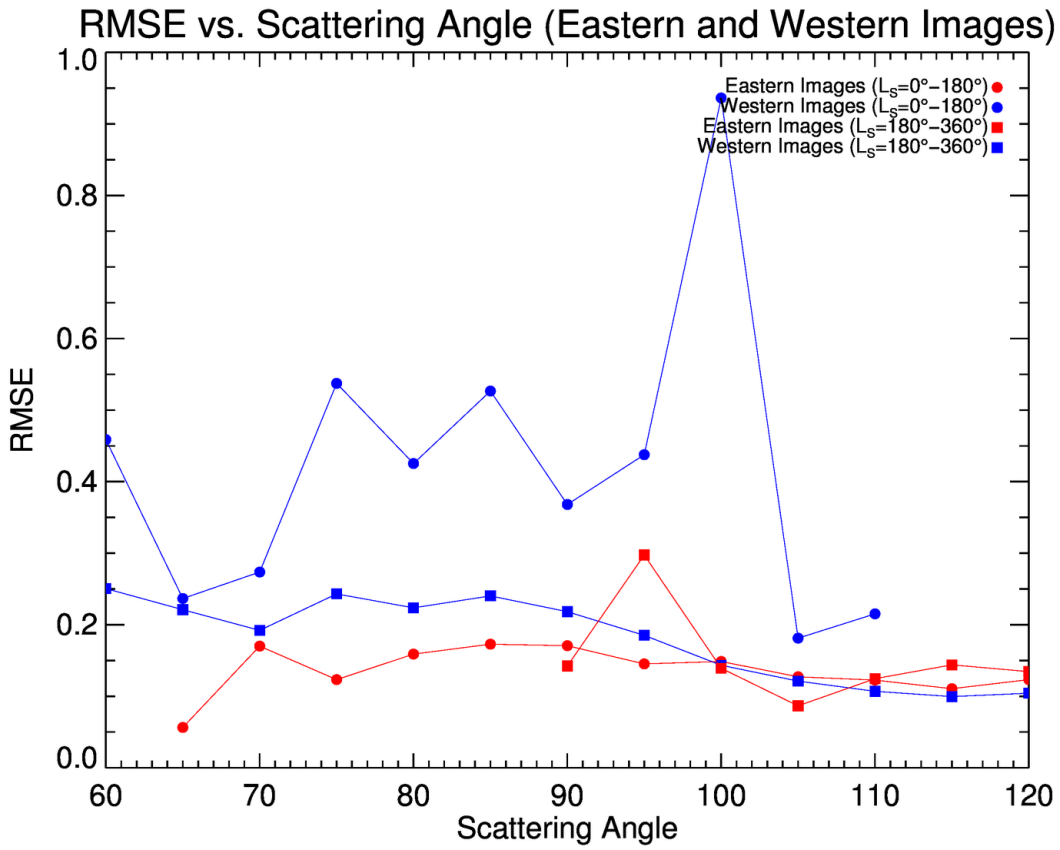

Figure 4.4: Root Mean Square Error (RMSE) vs. Scattering Angle. The different colors represent the directional pointing of the image, east-facing (red) and west-facing (blue), and the different shapes represent the season the image was acquired in, $L_S = 0 - 180°$ (circle) and $L_S = 180 - 360°$ (square).

measurement, is examined in Figure 4.4. This was done in order to show which angles produced a derived optical depth value with the smallest error and justify our reason for choosing a scattering angle of 105° as our standard. There is no significance choosing 105° as opposed to any of the other scattering angles within a ±5° range, as long as the selection process carefully considers what season the image was acquired in, or where the rover's camera was pointed relative to the Sun's location in the sky.

Figure 4.4 also demonstrates that throughout the Martian year, especially $L_S = 0 - 180°$, western images were often acquired too close to the Sun. This resulted in a higher overall RMS error that is observed in both sets of western images. Eastern Navcam sky images, on the other hand, appear to produce optical depth values that are in close agreement with Pancam results across a much wider range of scattering angles than western sky images. This is because these images tended to be focused on a region of sky that was further away from the Sun, and thus, more forgiving. Standard deviation and reduced χ^2 as a function of scattering angle were also looked at and used to further verify the conclusions made above.

We use a scattering angle of 105° as our reference and examine the data set further by performing a variety of statistical tests. An analysis including which low horizon sky images (western or eastern) to use in order to produce an accurate and consistent optical depth record was also done. Results from the observational campaign can be summarized in Table A.1 found in Appendix A. The Solar Elevation Angle and Derived Navcam Tau columns are a constructed by choosing the appropriate (i.e. seasonally correct) images. From sol 3579-3750, eastern sky images were used to construct the Solar Elevation Angle and Derived Navcam Tau columns, sol 3778-4048 use western sky images, and sol 4062-4248 use eastern sky images. This selection criteria is based on having the image boresight close to 90° away from the Sun as the

azimuth of sunset seasonally moves. The last column, Error, is simply the difference of the derived Navcam opacity from the observed Pancam opacity.

Sky opacities ranging from 0.391 to 1.64 were tested using the scattering model. The value of optical depth did not seem to have any affect on the model's ability to derive an accurate measurement when compared to the corresponding Pancam value. The standard deviation of the derived Navcam optical depth data set was found to be 0.239. When compared with the Pancam data set, the standard deviation of the residual error was measured to be 0.07. Taking the absolute value of the last column in Table A.1, the RMS error was also computed, with having a value of 0.124. The RMS error is a measure of the error around the regression line, in the same sense that the standard deviation is a measure of variability around the mean. Approximately 65% of the data was found to lie within one RMS error when a regression line was constructed. Using the results in Table A.1, a Navcam optical depth record was constructed as seen in Figure 4.5. The Pancam derivation, as reported in Lemmon et al. (2015) and the PDS archive, includes a correction for ½ optical depth on the windows, while the Navcam data are shown with no window-dust correction. We assume error bars to be the overall RMS error. The calculated RMS error was found to meet the performance objectives of the *InSight* mission (Mark Lemmon, personal communication).

To further demonstrate the robustness of the atmospheric scattering model, derived Navcam optical depth values were superimposed with the preliminary results generated from the database of synthetic sky images. The brightness profile in Figure 4.6 shows that the majority of derived data points are in close agreement and capture the same general pattern as the preliminary results, which were used to model the Martian sky. Several Navcam sky images did not exhibit a scattering angle of 90° for the selected elevation angles of 15° and 30°, which resulted in the inaccurate de-

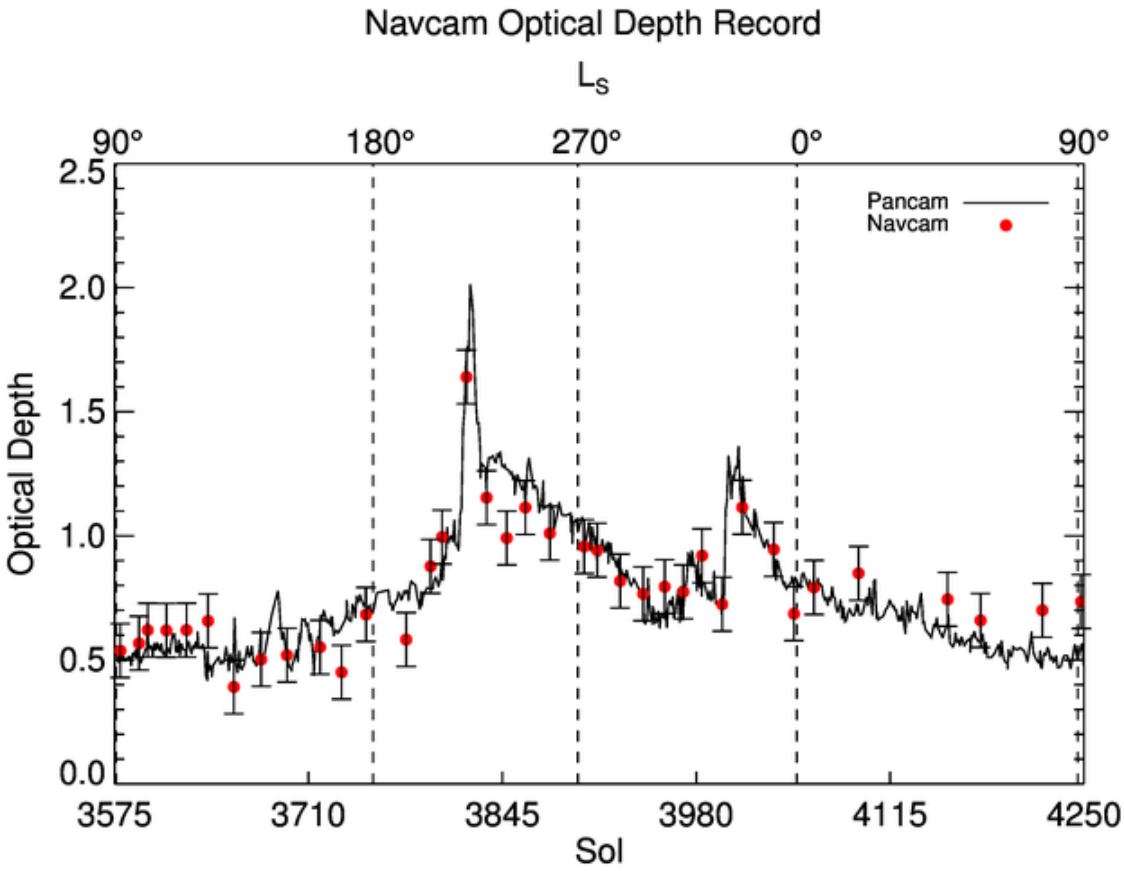

Figure 4.5: Derived optical depths are shown (red), and compared to the daily solar-filter optical depth record from Pancam (Lemmon, 2014). Error bars are the overall RMS error.

rivation of optical depth, and thus produced outlying data points. Nonetheless, this brightness profile demonstrates the strong correlation of radiance ratio with optical optical depth for the observed data. Furthermore, the strong correlation between these two parameters allows for a quick approximation if one is interested in knowing what the intensity ratio is for a specific opacity or vice versa. With the exception of a few minor instances, which are described in Section 5, we have shown that retrieving optical depth from Navcam non-solar sky images using a robust scattering model works to a high degree of accuracy. Even with dusty optics, the ratio method

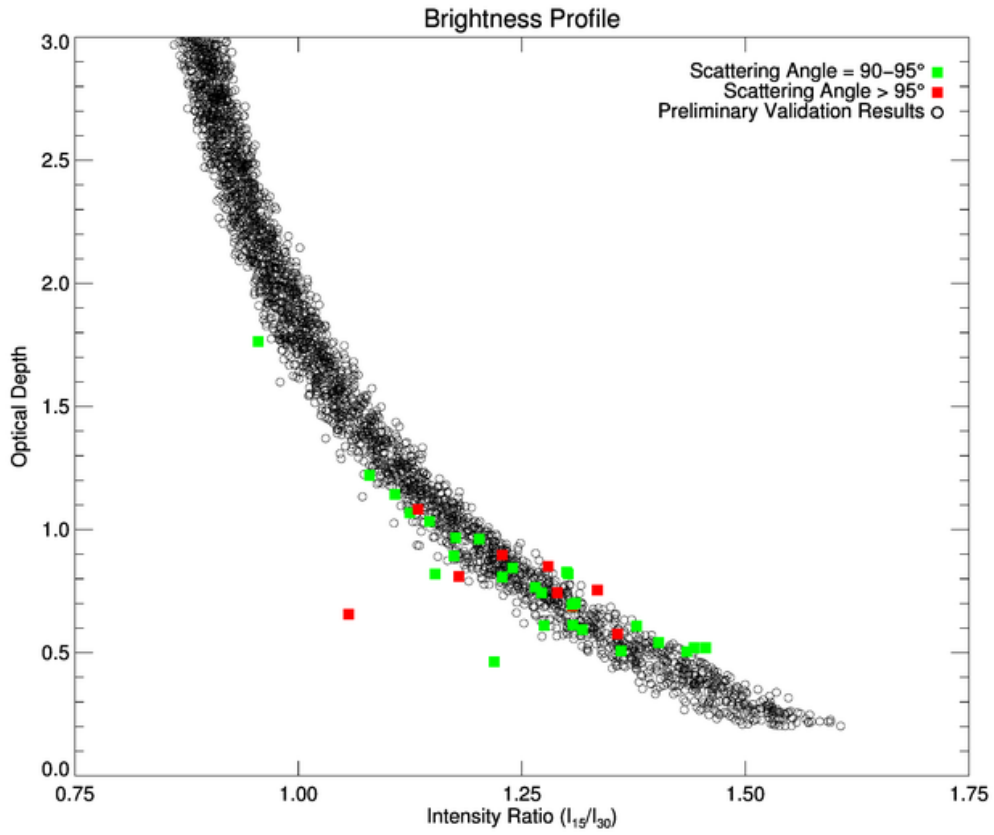

Figure 4.6: Derived Navcam optical depths superimposed with the preliminary validation results. Despite a few outlying data points, the model is able to fit the retrieved data to within a high degree of accuracy and shows the same strong correlation of radiance ratio with optical depth as the preliminary data resulting from the synthetic sky images.

employed by the scattering model is able to fit the model radiance profile to the image radiance profile with very little error.

The robustness of the scattering model originates from utilizing the optical and bulk scattering properties of the dust particles rather than the physical properties (shape, composition, etc.). Thus, no specific information about the dust itself is

needed, other than aerosol optical depth, for the scattering model's ratio method to produce high fidelity results. Assuming no bias and that the RMS error of 0.124 can be attributed to a combination of the (unknown) error of the model fitting process and the intrinsic Pancam error of 0.058, we can estimate that the intrinsic Navcam error is 0.084.

4.3 Error Investigation

After a statistical analysis was performed on the data set, an investigation searching for possible sources of error was undertaken. Model error was plotted against a variety of parameters including model tau, solar elevation angle, and sol. Solar elevation angle as a function of sol was also examined, searching for a potential relationship between the two variables. As seen in Figure 4.7, however, no correlation was found between any of these parameters.

Once it was established that optical depth values for a scattering angle of 105° were the data set of record, a closer look was taken to understand how the error in derived model tau affected the logarithmic sky intensity generated by DISORT. A test, therefore, using perturbed model tau and radiance as a function of elevation angle was used to investigate error propagation. In addition to model sensitivity, this test was also used to determine whether or not the derived optical depth values obtained from a scattering angle of 105° were in fact the best values (i.e. had the smallest error difference) when looking at an elevation profile and comparing the results with daily solar imaging observations from Pancam. Figure 4.8 shows the acquired Navcam sky image and resulting elevation profile from the scattering model. The best fit series (black diamonds) is the difference in sky radiance resulting from the derived optical depth value which produced the smallest error and the sky radiance computed from the image file. This comparison of model radiance with image

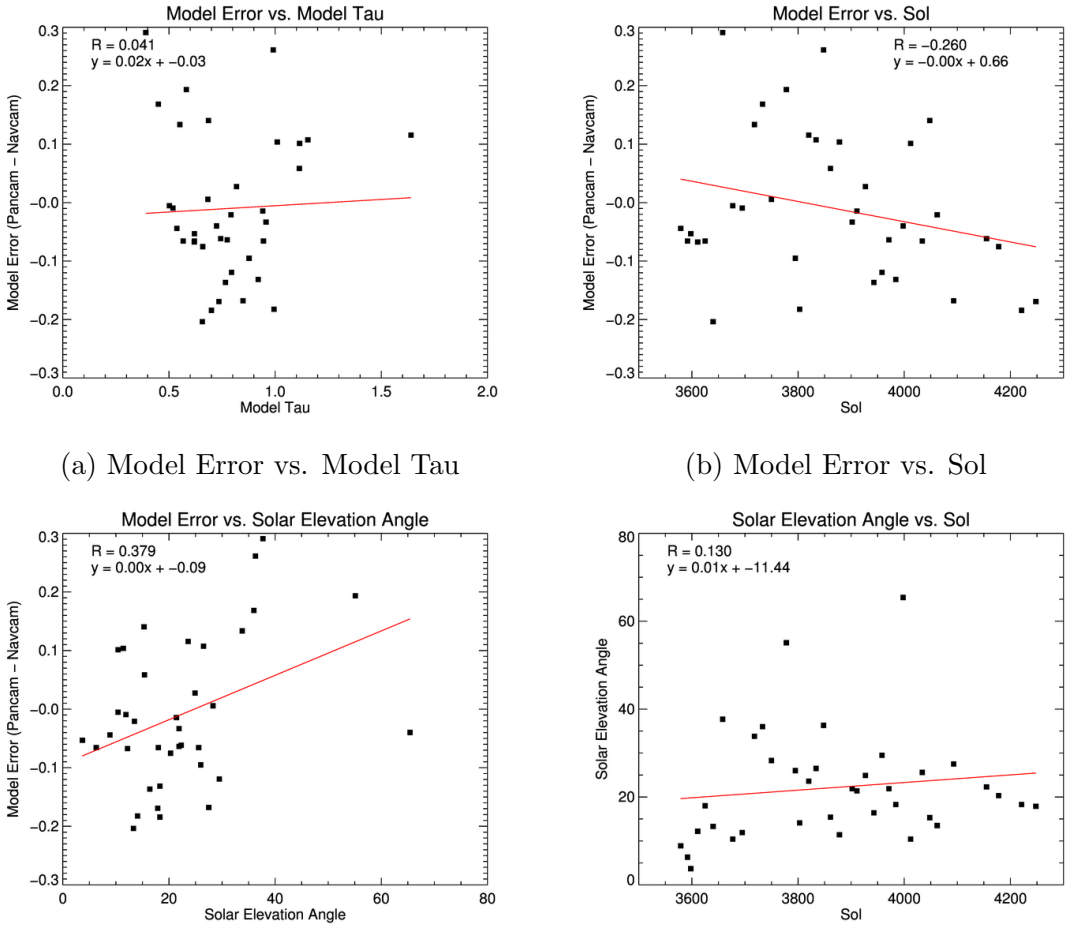

(a) Model Error vs. Model Tau

(b) Model Error vs. Sol

(c) Model Error vs. Elevation Angle

(d) Elevation Angle vs. Sol

Figure 4.7: Model error plotted against various parameters in an attempt to find possible correlations hidden within the data, and thus, potential sources of error and error propagation.

radiance is done several times by perturbing the best fit optical depth value (shades of blue and green diamonds) to show the accuracy and robustness of the scattering model. The perturbed fits were computed by offsetting the best fit value by a standard deviation of ± 1 (0.239) and ± 2 (0.478) respectively. A closer look at Figure 4.8 reveals that the best fit series for each sol captures the observed Pancam measurements very well, while the perturbed series do much worse and begin deviating far

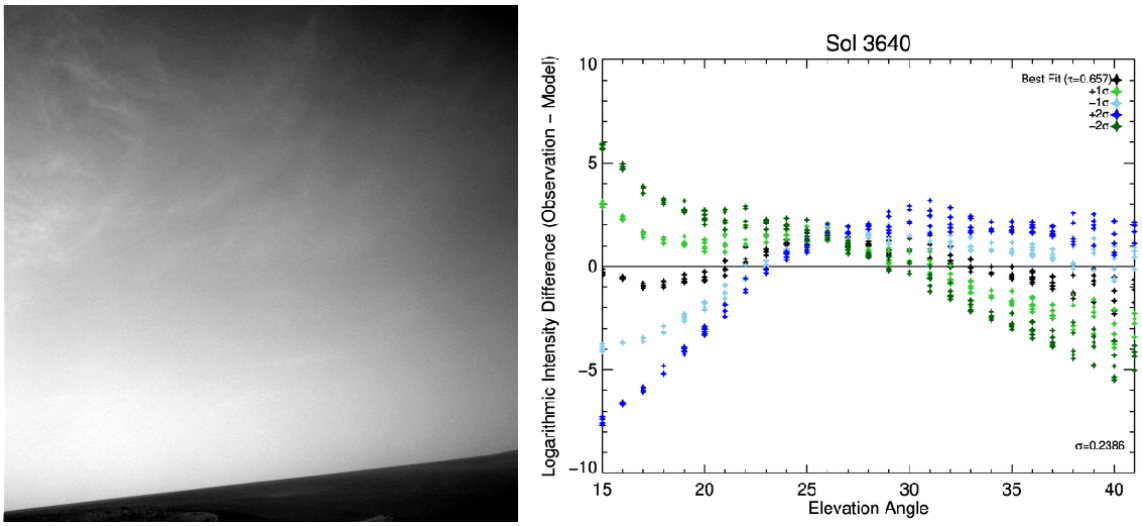

(a) Navcam sky image and model error with perturbed fits for sol 3640

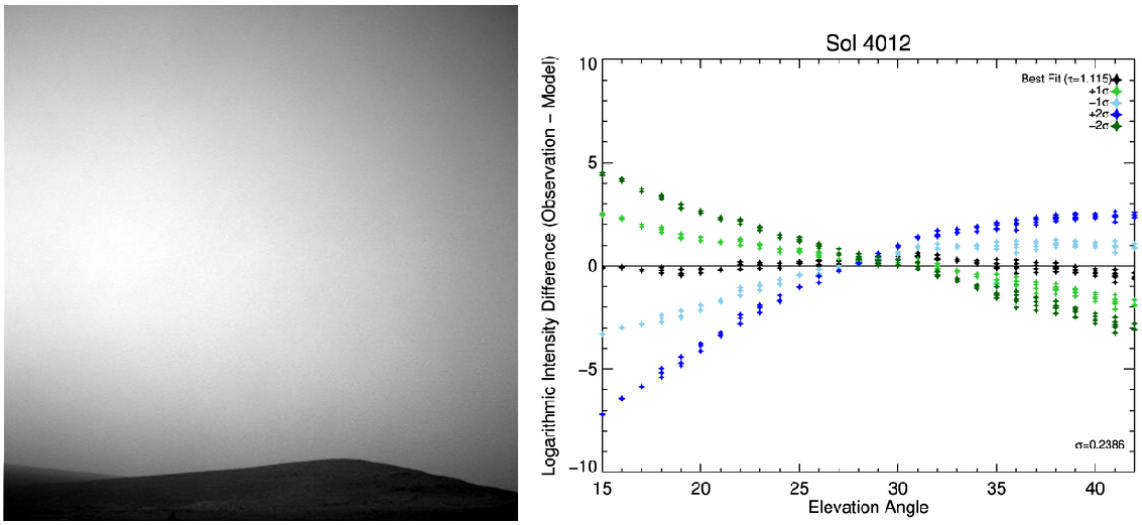

(b) Navcam sky image and model error with perturbed fits for sol 4012

Figure 4.8: Elevation profiles showing the logarithmic difference in sky intensity between the image sky and model sky. The best fit series (black diamonds) is the sky radiance resulting from the derived optical depth value which produced the smallest error and subtracted from the sky radiance computed from the image file. This comparison is done several times using perturbed fits (shades of blue and green diamonds) to show the accuracy of the scattering model.

away from what is actually observed. The cloudy day (sol 3640) doesn't do quite as well when matching the derived data set with the observed Pancam record due to

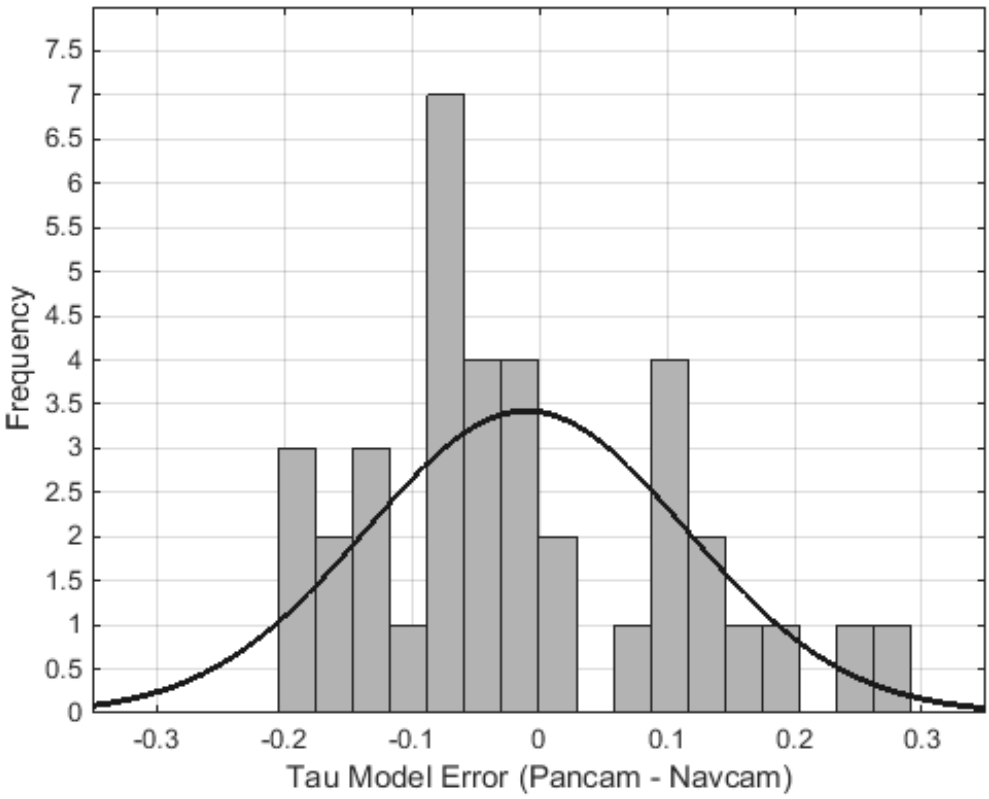

Figure 4.9: Histogram of model tau error for a scattering angle of 105°. A bin size of 17 is used with 1-sigma occurring at ±0.239.

the spatial variability of the clouds since the scattering model assumes a uniform, homogeneous sky.

The histogram in Figure 4.9 shows the distribution of tau model error with a Gaussian distribution superimposed. Given the truly random nature of the scattering parameters, the model error follows a fairly normal distribution, adhering to the central limit theorem. The majority of tau model error is centered around 0, indicating the high accuracy of the scattering model. Approximately 97% of the data set has a tau model error that that occurs within 1-sigma (±0.239). The purpose

of constructing a histogram was to see if there was any sort of bias hidden in the derived optical depth data set. Using a bin size of 17, the resulting histogram in Figure 4.9 confirms that tau model error is completely random with no indication of any bias.

5. DISCUSSION

5.1 Seasonal Variation of Optical Depth

The derived optical depth values obtained from Navcam were able to capture the seasonal variability of optical depth over the course of about one Mars year. The TES climatology (Smith, 2004) and previous observations over the last 5 Mars years (Lemmon et al., 2015) would suggest that optical depths would decline into aphelion season, rise slightly near $L_S = 135°$, and become dusty during perihelion season, with dust increases around $L_S = 180°$, $L_S = 220°$, and $L_S = 320°$. Other than a few slight variations, this typical seasonal pattern in optical depth was observed once again at the *Opportunity* site during this simulation-based imaging campaign. Figure 5.1 presents a climatological optical depth record created from 5 Mars years worth of data. The derived optical depth record generated during this campaign is overlaid on a pseudo-composite optical depth record created from minimum/maximum sky opacity values collected at the *Opportunity* site from the last 5 Mars years. Throughout most of the year, the derived optical depth record stays fairly close to the shaded band of optical depth values. Patchy clouds, which are discussed in the next section, and dusty camera optics are among the few things responsible for small deviations in the derived Navcam optical depth record seen in Figure 4.4. Navcam sky images were acquired starting on $L_S = 91.1°$, during the relatively dust-free aphelion season. Beginning around $L_S = 149.5°$, a gradual increase in opacity was observed, hinting at the possibility of an inbound dust storm. By $L_S = 220.0°$, a regional dust storm had formed over Cape Tribulation on the western rim of Endeavor crater with optical depth abruptly rising to a value of 1.640. This was followed by a steady, but relatively steep decline in optical depth to a local minimum of 0.766 occurring on sol

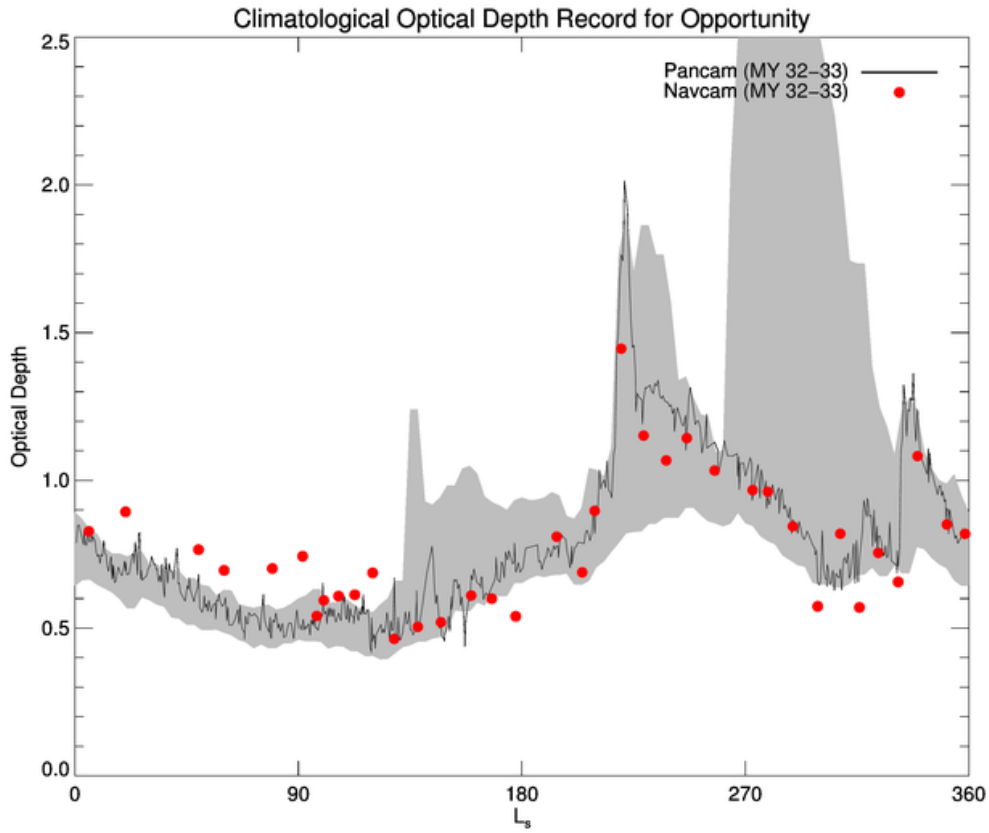

Figure 5.1: Climatological optical depth record at *Opportunity* site. The shaded region represents 97.5% of all tau values that were collected over 5 Mars years. The black line is the Pancam optical depth record for MY 32-33 and the red dots are the derived optical depth record from Navcam.

3943. Such a decrease translates to a change of 0.71% per sol, which is consistent with initial reports of 0.6-0.7% per sol by (Lemmon et al., 2004). Regional-scale dust storms like this one occur every Martian year during the dusty season, particularly near $L_S = 225°$ and 315°, when cross-equatorial flushing dust storms occur (Smith, 2008).

After this fairly substantial decrease in optical depth, a short-lived fluctuation

of $\Delta\tau = 0.2$ occurs around $L_S = 320.0°$ before jumping to $\tau = 1.115$ around $L_S = 340.0°$. Once again this sharp rise in optical depth is followed by a steady decline that persists until the end of MY 32 and continues through MY 33 until $L_S = 90.0°$ when non-solar Navcam sky observations ceased and one Mars year worth of data had been collected. During this relatively inactive time period spanning from $L_S = 0°$- 180°, there are no very large dust storms and the atmosphere is characterized by a much lower background level of dust optical depth. Local dust storm activity is confined largely to the region near the edge of the seasonal polar ice caps, especially along the retreating north cap during northern spring, and along the southern cap at the end of southern winter (Smith, 2008).

Throughout most of the imaging campaign, the sky opacity derived from non-solar Navcam sky images captured the same seasonal changes in dust loading and followed the same general pattern as measured by Pancam. The derived optical depth measurements resulting from the scattering model's ratio method have been shown to be precise enough to detect small changes in sky opacity, allowing a detailed and accurate optical depth record to be constructed. Creating climatological optical depth records like the one in Figure 5.1, therefore, are not only important for understanding seasonal changes in dust loading, but may also provide engineers with the necessary information to ensure the safety of solar-powered rovers and landers during a mission.

5.2 Clouds

In addition to dust, aerosols in the form of condensate clouds occur frequently on Mars. During the aphelion season, condensate clouds made up of water ice and CO_2 ice are intermittently observed by both ground and orbiting spacecraft. Such clouds contributed to the observed opacity at the *Opportunity* site during L_S=105-

119°, with peak activity occurring near L_S=119°. Wispy cloud formations were also observed around L_S=20°.

The Navcam images acquired by *Opportunity* are not indicative as to the cloud composition. Water ice is likely, however, given the aphelion cloud belt was at its maximum extent over the *Opportunity* site during this time period. Water ice hazes may have been present as well. Nonetheless, it is during this seasonal phenomenon that several data points are seen to lie above the general trend characterized by Pancam measurements as shown in Figure 5.1

This low-latitude belt of clouds described above appears to repeat every year with very similar amplitude and spatial distribution. The cloud belt begins to form around L_S=0°, building to maximum intensity and spatial coverage by about L_S=80°. The cloud belt has significant optical depth between 10°S and 30°N latitude, with higher optical depth over topographic highs. Repeated imaging of the sky shows that clouds are common at the *Opportunity* site between L_S=20°-140°, and often have a morphology similar to terrestrial cirrus clouds (Smith, 2008). The optical depth of water ice clouds is often anticorrelated with that of dust. Whereas large dust storms form preferentially during the dusty, perihelion season (L_S=180°-360°), the greatest extent of water ice clouds are observed during the cooler aphelion season (L_S=0°-180°) and in the polar regions in the winter hemisphere (Tamppari et al., 2000; Pearl et al., 2001; Liu et al., 2003; Smith, 2004).

Despite their relatively small spatial coverage, ice clouds on Mars have a significant effect on the global water cycle. The radiative effects of water ice clouds on the temperature profile of Mars can also be quite substantial. Infrared properties inherent of water ice, combined with the low-mass of the Martian atmosphere, can lead to strong thermal cooling by water ice clouds during the night (Smith, 2008). Indirectly these clouds may also play a critical role in dynamics of the planet.

In addition to affecting the Martian climate, clouds also affect sky brightness. This is particularly problematic when clouds, especially those that have a wispy-like structure, are present in Navcam's FOV. This is because the scattering model assumes horizontally homogeneous scatterers, creating a layer of uniform sky brightness. Depending upon spatial coverage, discrete cloud formations can result in derived optical depth values deviating as much as 1-sigma from what was observed with Pancam. Such occurrences are rare however, as clouds were only noticeably visible in 2 of the 37 observations that were made with the Navcam instrument. Despite the scattering model having some difficulty interpreting cloudy images, it still remains fairly robust and is able to derive optical depth values that fit closely to Pancam observations taken on the same sol.

6. CONCLUSIONS AND FUTURE WORK

A precise optical depth record for the *Opportunity* rover has been created using non-solar sky images from the onboard engineering cameras and a robust scattering model. The data set spans approximately one Mars year, including periods of local and regional dust storms as well as the intermittent appearance of discrete cloud formations. Even with dusty optics, this simulation-based imaging strategy retrieved optical depth with a high degree of accuracy, with an intrinsic Navcam error of 0.084 and RMS error of 0.124. This study not only characterizes the versatility of Navcam, but also illustrates the robustness of the scattering model.

The scattering model is not without its limitations, however, as was observed when the camera was pointed too close to the Sun or clouds were in the camera's FOV. Future work includes the removal of camera artifacts resulting from instrumental reflection and pronounced cloud formations from the sky images in order to obtain a more accurate optical depth measurement from the scattering model.

With planetary science budgets getting ever tighter, it is not always possible to equip landers and rovers with science cameras that include dedicated solar filters. The encouraging results obtained from the scattering model's robust ratio method are not only important for *InSight*, but other future missions equipped with similar cameras as well. Besides providing significant contributions in terms of spacecraft cost and development, these results will also benefit mission operations and planning. Furthermore, innovative imaging techniques, such as the one described in this thesis, also provide rovers and landers with greater functionality. Despite their basic purpose, engineering cameras have the ability to provide a good estimate of the amount of dust in the Martian atmosphere when coupled with a robust scattering model.

REFERENCES

Ahrens, D. C., *Meteorology Today: An Introduction to Weather, Climate, and the Environment*, 8 ed., Thomson Brooks/Cole, Belmont, CA, 2007.

Alexander, D. A., R. G. Deen, P. M. Andres, P. Zamani, H. B. Mortensen, et al., Processing of Mars Exploration Rover imagery for science and operations planning, *Journal of Geophysical Research: Planets*, *111*(E2), 1–21, 2006.

Bell, J. F., J. Joseph, J. N. Sohl-Dickstein, H. M. Arneson, M. J. Johnson, et al., In-flight calibration and performance of the Mars Exploration Rover panoramic camera (Pancam) instruments, *Journal of Geophysical Research: Planets*, *111*(E2), 1–113, 2006.

Bell, J. F., H. Y. McSween, J. A. Crisp, R. V. Morris, S. L. Murchie, et al., Mineralogic and compositional properties of Martian soil and dust: results from Mars Pathfinder, *Journal of Geophysical Research: Planets*, *105*(E1), 1721–1755, 2000.

Bell, J. F., S. W. Squyres, K. E. Herkenhoff, J. N. Maki, H. M. Arneson, et al., Mars Exploration Rover Athena panoramic camera (Pancam) investigation, *Journal of Geophysical Research: Planets*, *108*(E12), 1–30, 2003.

Cantor, B. A., MOC observations of the 2001 Mars planet-encircling dust storm, *Icarus*, *186*(1), 60–96, 2007.

Chlek, P., and G. Grams, Scattering by nonspherical particles and optical properties of Martian dust, *Icarus*, *36*(2), 198–203, 1978.

Colburn, D., J. Pollack, and R. Haberle, Diurnal variations in optical depth at Mars, *Icarus*, *79*(1), 159–189, 1989.

Crisp, D., A. Pathare, and R. Ewell, The performance of gallium arsenide/germanium solar cells at the Martian surface, *Acta Astronautica*, *54*(2), 83 – 101, 2004.

Di, R., K.and Li, CAHVOR camera model and its photogrammetric conversion for planetary applications, *Journal of Geophysical Research: Planets*, *109*(E4), 1–9, 2004.

Eliason, E., B. Castalia, S. Mattson, R. Heyd, K. Becker, et al., Software interface specification for HiRISE reduced data record products, *MRO JPL Document D-32006*, 2009.

Gennery, D. B., *Calibration and Orientation of Cameras in Computer Vision*, chap. Least-squares camera calibration including lens distortion and automatic editing of calibration points, pp. 123–136, Springer Berlin Heidelberg, Berlin, Heidelberg, 2001.

Greeley, R., D. A. Waller, N. A. Cabrol, G. A. Landis, M. T. Lemmon, et al., Gusev Crater, Mars: Observations of three dust devil seasons, *Journal of Geophysical Research: Planets*, *115*(E7), 1–18, 2010.

Greeley, R., P. L. Whelley, R. E. Arvidson, N. A. Cabrol, D. J. Foley, et al., Active dust devils in Gusev Crater, Mars: Observations from the Mars Exploration Rover Spirit, *Journal of Geophysical Research: Planets*, *111*(E12), 1–16, 2006.

Hansen, J. E., and L. D. Travis, Light scattering in planetary atmospheres, *Space Science Reviews*, *16*(4), 527–610, 1974.

Hodkinson, J. R., and I. Greenleaves, Computations of light-scattering and extinction by spheres according to diffraction and geometrical optics, and some comparisons with the Mie theory, *Journal of the Optical Society of America*, *53*(5), 577–588, 1963.

Johnson, J. R., W. M. Grundy, and M. T. Lemmon, Dust deposition at the Mars Pathfinder landing site: observations and modeling of visible/near-infrared spectra, *Icarus*, *163*(2), 330–346, 2003.

Kinch, K. M., J. F. Bell, W. Goetz, J. R. Johnson, J. Joseph, et al., Dust deposition

on the decks of the Mars Exploration Rovers: 10 years of dust dynamics on the panoramic camera calibration targets, *Earth and Space Science*, *2*(5), 144–172, 2015.

Korablev, O., V. Krasnopolsky, A. Rodin, and E. Chassefire, Vertical structure of Martian dust measured by solar infrared occultations from the Phobos spacecraft, *Icarus*, *102*(1), 76–87, 1993.

Landis, G. A., and P. P. Jenkins, Measurement of the settling rate of atmospheric dust on Mars by the MAE instrument on Mars Pathfinder, *Journal of Geophysical Research: Planets*, *105*(E1), 1855–1857, 2000.

Lemmon, M. T., The Mars Science Laboratory optical depth record, *LPI Contributions*, *1791*, 1338, 2014.

Lemmon, M. T., M. J. Wolff, J. F. B. III, M. D. Smith, B. A. Cantor, et al., Dust aerosol, clouds, and the atmospheric optical depth record over 5 Mars years of the Mars Exploration Rover mission, *Icarus*, *251*, 96–111, 2015.

Lemmon, M. T., M. J. Wolff, M. D. Smith, R. T. Clancy, D. Banfield, et al., Atmospheric imaging results from the Mars Exploration Rovers: Spirit and Opportunity, *Science*, *306*(5702), 1753–1756, 2004.

Liu, J., M. I. Richardson, and R. J. Wilson, An assessment of the global, seasonal, and interannual spacecraft record of Martian climate in the thermal infrared, *Journal of Geophysical Research: Planets*, *108*(E8), 1–38, 2003.

Maki, J. N., J. F. Bell, K. E. Herkenhoff, S. W. Squyres, A. Kiely, et al., Mars Exploration Rover engineering cameras, *Journal of Geophysical Research: Planets*, *108*(E12), 1–24, 2003.

Malin, M. C., and K. S. Edgett, Mars Global Surveyor Mars Orbiter Camera: interplanetary cruise through primary mission, *Journal of Geophysical Research: Planets*, *106*(E10), 23,429–23,570, 2001.

Markiewicz, W. J., R. M. Sablotny, H. U. Keller, N. Thomas, D. Titov, et al., Optical properties of the Martian aerosols as derived from Imager for Mars Pathfinder midday sky brightness data, *Journal of Geophysical Research: Planets*, *104*(E4), 9009–9017, 1999.

Markwardt, C. B., Non-linear least-squares fitting in IDL with MPFIT, in *Astronomical Data Analysis Software and Systems XVIII*, *Astronomical Society of the Pacific Conference Series*, vol. 411, edited by D. A. Bohlender, D. Durand, and P. Dowler, p. 251, 2009.

Martin, L. J., and R. W. Zurek, An analysis of the history of dust activity on Mars, *Journal of Geophysical Research: Planets*, *98*(E2), 3221–3246, 1993.

Montabone, L., F. Forget, E. Millour, R. Wilson, S. Lewis, et al., Eight-year climatology of dust optical depth on Mars, *Icarus*, *251*, 65–95, 2015.

Moores, J. E., M. T. Lemmon, H. Kahanp, S. C. Rafkin, R. Francis, et al., Observational evidence of a suppressed planetary boundary layer in northern Gale Crater, Mars as seen by the Navcam instrument onboard the Mars Science Laboratory rover, *Icarus*, *249*, 129–142, 2015a.

Moores, J. E., M. T. Lemmon, S. C. Rafkin, R. Francis, J. Pla-Garcia, et al., Atmospheric movies acquired at the Mars Science Laboratory landing site: cloud morphology, frequency and significance to the Gale Crater water cycle and Phoenix mission results, *Advances in Space Research*, *55*(9), 2217–2238, 2015b.

Moré, J. J., and D. C. Sorensen, The MINPACK project, *Sources and Development of Mathematical Software*, pp. 88–111, 1984.

Morris, R. V., G. Klingelhfer, C. Schrder, D. S. Rodionov, A. Yen, et al., Mössbauer mineralogy of rock, soil, and dust at Gusev Crater, Mars: Spirit's journey through weakly altered olivine basalt on the plains and pervasively altered basalt in the Columbia Hills, *Journal of Geophysical Research: Planets*, *111*(E2), 1–28, 2006a.

Morris, R. V., G. Klingelhfer, C. Schrder, D. S. Rodionov, A. Yen, et al., Mössbauer mineralogy of rock, soil, and dust at Meridiani Planum, Mars: Opportunity's journey across sulfate-rich outcrop, basaltic sand and dust, and hematite lag deposits, *Journal of Geophysical Research: Planets*, *111*(E12), 1–27, 2006b.

NASA/JPL-Caltech/Cornell, PIA03272: "Still shining after all this time (vertical)"", 2006.

NASA/JPL-Caltech/Cornell, PIA09935: "Dust storm time lapse shows Opportunity's skies darken"", 2007a.

NASA/JPL-Caltech/Cornell, PIA10128: "Dusty solar panels on Spirit"", 2007b.

Pearl, J. C., M. D. Smith, B. J. Conrath, J. L. Bandfield, and P. R. Christensen, Observations of Martian ice clouds by the Mars Global Surveyor Thermal Emission Spectrometer: the first Martian year, *Journal of Geophysical Research: Planets*, *106*(E6), 12,325–12,338, 2001.

Pollack, J. B., and J. N. Cuzzi, Scattering by nonspherical particles of size comparable to a wavelength: a new semi-empirical theory and its application to tropospheric aerosols, *Journal of the Atmospheric Sciences*, *37*(4), 868–881, 1980.

Pollack, J. B., M. E. Ockert-Bell, and M. K. Shepard, Viking lander image analysis of Martian atmospheric dust, *Journal of Geophysical Research: Planets*, *100*(E3), 5235–5250, 1995.

Shaw, A., M. J. Wolff, F. P. Seelos, S. M. Wiseman, and S. Cull, Surface scattering properties at the Opportunity Mars rover's traverse region measured by CRISM, *Journal of Geophysical Research: Planets*, *118*(8), 1699–1717, 2013.

Smith, M. D., Interannual variability in TES atmospheric observations of Mars during 19992003, *Icarus*, *167*(1), 148–165, 2004.

Smith, M. D., Spacecraft observations of the Martian atmosphere, *Annual Review of Earth and Planetary Sciences*, *36*(1), 191–219, 2008.

Smith, M. D., and M. J. Wolff, Dust aerosol particle size and shape using MER NAVCAM and PANCAM sky imaging, in *Mars Atmosphere: Modelling and Observation, 5th International Workshop*, p. 2101, 2014.

Smith, M. D., M. J. Wolff, N. Spanovich, A. Ghosh, D. Banfield, et al., One Martian year of atmospheric observations using MER Mini-TES, *Journal of Geophysical Research: Planets*, *111*(E12), 1–16, 2006.

Smith, P. H., and M. T. Lemmon, Opacity of the Martian atmosphere measured by the imager for Mars Pathfinder, *Journal of Geophysical Research: Planets*, *104*(E4), 8975–8985, 1999.

Soderblom, J. M., Properties of Martian soils, rocks, and atmospheric dust derived from analysis of Hubble Space Telescope and Mars Exploration Rover data, Ph.D. thesis, Cornell University, Ithaca, NY, 2007.

Soderblom, J. M., J. F. Bell, J. R. Johnson, J. Joseph, and M. J. Wolff, Mars Exploration Rover navigation camera in-flight calibration, *Journal of Geophysical Research: Planets*, *113*(E6), 3003–3187, 2008.

Squyres, S. W., R. E. Arvidson, E. T. Baumgartner, J. F. Bell, P. R. Christensen, et al., Athena Mars rover science investigation, *Journal of Geophysical Research: Planets*, *108*(E12), 1–21, 2003.

Stamnes, K., S.-C. Tsay, W. Wiscombe, and K. Jayaweera, Numerically stable algorithm for discrete-ordinate-method radiative transfer in multiple scattering and emitting layered media, *Applied Optics*, *27*(12), 2502–2509, 1988.

Stella, P., and J. Herman, The Mars surface environment and solar array performance, in *Photovoltaic Specialists Conference (PVSC), 2010 35th IEEE*, pp. 2631–2635, 2010.

Tamppari, L. K., R. W. Zurek, and D. A. Paige, Viking era water-ice clouds, *Journal of Geophysical Research: Planets*, *105*(E2), 4087–4107, 2000.

Tomasko, M. G., L. R. Doose, M. T. Lemmon, P. H. Smith, and E. Wegryn, Properties of dust in the Martian atmosphere from the imager on Mars Pathfinder, *Journal of Geophysical Research: Planets*, *104*(E4), 8987–9007, 1999.

Toon, O. B., J. B. Pollack, and C. Sagan, Physical properties of the particles composing the Martian dust storm of 1971-1972, *Icarus*, *30*(4), 663–696, 1977.

van de Hulst, H. C., Light scattering by small particles, *Quarterly Journal of the Royal Meteorological Society*, *84*(360), 198–199, 1958.

Wiscombe, W. J., The Delta-M method: rapid yet accurate radiative flux calculations for strongly asymmetric phase functions, *Journal of the Atmospheric Sciences*, *34*(9), 1408–1422, 1977.

Wolff, M. J., S. W. Lee, R. T. Clancy, L. J. Martin, J. F. Bell, et al., 1995 observations of Martian dust storms using the Hubble Space Telescope, *Journal of Geophysical Research: Planets*, *102*(E1), 1679–1692, 1997.

Wolff, M. J., M. D. Smith, R. T. Clancy, R. Arvidson, M. Kahre, et al., Wavelength dependence of dust aerosol single scattering albedo as observed by the Compact Reconnaissance Imaging Spectrometer, *Journal of Geophysical Research: Planets*, *114*(E2), 1–17, 2009.

Yakimovsky, Y., and R. Cunningham, A system for extracting three-dimensional measurements from a stereo pair of TV cameras, *Computer Graphics and Image Processing*, *7*(2), 195–210, 1978.

APPENDIX A

NAVCAM *INSIGHT* TAU RESULTS

Table A.1: Derived Navcam *InSight* tau results with observed Pancam measurements acquired on the same sol for comparison.

Sol	**Solar Elevation Angle (°)**	**Derived Navcam Tau**	**Pancam Tau**	**Error**
3579	8.9	0.537	0.493	-0.044
3592	6.3	0.567	0.501	-0.066
3598	3.7	0.620	0.567	-0.053
3611	12.2	0.619	0.552	-0.067
3625	18.0	0.620	0.554	-0.066
3640	13.3	0.657	0.453	-0.204
3658	37.7	0.391	0.682	0.291
3677	10.4	0.502	0.497	-0.005
3695	11.9	0.519	0.510	-0.009
3718	33.8	0.551	0.685	0.134
3733	36.0	0.450	0.619	0.169
3750	28.3	0.683	0.689	0.006
3778	55.1	0.582	0.775	0.193
3795	26.0	0.877	0.782	-0.095
3803	14.1	0.995	0.813	-0.182
3820	23.6	1.640	1.756	0.116
3834	26.5	1.154	1.261	0.107
3848	36.3	0.991	1.252	0.261

Continued on next page

Table A.1 – *Continued from previous page*

Sol	**Solar Elevation Angle (°)**	**Derived Navcam Tau**	**Pancam Tau**	**Error**
3861	15.4	1.114	1.173	0.059
3878	11.4	1.010	1.114	0.104
3902	21.9	0.957	0.924	-0.033
3911	21.4	0.942	0.928	-0.014
3927	24.9	0.818	0.845	0.027
3943	16.4	0.766	0.629	-0.137
3958	29.5	0.795	0.676	-0.119
3971	21.9	0.774	0.710	-0.064
3984	18.3	0.920	0.789	-0.131
3998	65.4	0.724	0.684	-0.040
4012	10.4	1.115	1.216	0.101
4034	25.6	0.945	0.879	-0.066
4048	15.3	0.686	0.826	0.140
4062	13.5	0.792	0.771	-0.021
4093	27.5	0.849	0.681	-0.168
4155	22.3	0.744	0.682	-0.062
4178	20.3	0.659	0.584	-0.075
4221	18.3	0.700	0.516	-0.184
4248	17.9	0.735	0.566	-0.169